UNIVERSITY OF CALIFORNIA,
IRVINE

Numerical Investigation of Bubble Behaviors in Saturated Pool Boiling

THESIS

submitted in partial satisfaction of the requirements
for the degree of

MASTER OF SCIENCE

in Mechanical and Aerospace Engineering

by

Shuai Hao

Thesis Committee:
Assistant Professor Yoonjin Won, Chair
Associate Professor Yun Wang
Professor Feng Liu

2018

TABLE OF CONTENTS

LIST OF FIGURES

LIST OF TABLES

ACKNOWLEDGMENTS

I would like to express the deepest appreciation to my committee chair, Professor Yoonjin Won, who inspires my research interest in multi-phase flow and heat transfer. The suggestions and encouragement from her give me confidence and progress throughout my study in Master period. Without her guidance and persistent help, this dissertation would not have been possible.

I would like to thank my committee members, Professor Yun Wang and Professor Feng Liu, whose work in the field of computational fluid dynamics (CFD) as well as heat and mass transfer provides me deep insights for the mathematical models used in this dissertation.

In addition, a thank you to my colleagues, Cheng-Hui Lin and Shiwei Zhang who help me a lot for the pool boiling experiment and the high-speed camera operation. Also, I would like to thank all members of UCI Won Lab. Sharing and discussing the research experience with them improve my knowledge background for boiling heat transfer and bubble simulation.

ABSTRACT OF THE THESIS

Numerical Investigation of Bubble Behaviors in Saturated Pool Boiling

By

Shuai Hao

Master of Science in Mechanical and Aerospace Engineering

University of California, Irvine, 2015

Assistant Professor Yoonjin Won, Chair

Vapor bubble behaviors under saturated pool boiling are investigated numerically and experimentally. For this, bubble dynamics such as the growth and detachment processes are simulated and discussed. The impacts of contact angle and surface structures on bubble dynamics as well as heat transfer performances are also presented. In this process, conservation equations of mass, momentum, and energy are numerically solved by commercial software ANSYS Fluent 18.1. In particular, the bubble departure diameters on flat heated surfaces are compared with theoretical model and experiments. Bubble period and wall heat flux are closely related to the velocity field around the contact line region. The numerical results also show that for a bubble growing on pillar surface, flow field around the pillar plays a significant role in the variation of bubble shape as well as an enhanced wall heat flux. Time-evolution images of single bubble evolution in pool boiling experiments are captured through a high-speed camera. Bubble behaviors from experiment and simulation show a good consistency.

CHAPTER 1. INTRODUCTION

With the rapid development of electronic devices in recent decades, heat flux generated from small devices shows the unprecedented increment. Therefore, traditional heat transfer methods like natural and forced convection using single phases would not be able to meet the heat transfer requirements in the near future. In response, boiling heat transfer gets more interest because of its great heat transfer performances in recent years. Boiling is a phase change process in which vapor bubbles are formed either on a heated surface or in a superheated liquid layer adjacent to the heated surface [1]. Boiling can generally be categorized into two classifications: pool boiling and forced flow boiling. Pool boiling refers to boiling under natural convection conditions, whereas force flow boiling means liquid flow over the heated surface is imposed by external forces.

Boiling heat transfer characteristics was firstly investigated by Shiro Nukiyama in 1934 [2]. After his pioneering work, boiling heat transfer has received considerable attention in the past decades. A typical boiling curve for saturated pool boiling of water at atmospheric pressure is shown in figure 1-1. With the increment of wall superheat, four stages of boiling (natural convection, nucleate boiling, transition boiling, and film boiling) have been observed. While wall superheat is below a specific value (usually 5^{o}C), no bubble appears at the heating surface, which is defined as natural convection. With the increment of wall temperature, bubbles start to nucleate at active nucleation cavities, which is called the nucleate boiling. This specific wall superheat that identifies nucleate boiling is called the onset of nucleate boiling (ONB), as indicated as point A in figure 1-1. Bubbles act individually in the region between point A and B. In region B-C, the strong interaction between vapor bubbles will subsequently form vapor jets or columns due to the higher bubble frequency. Once, wall heat flux reaches a maximum value at point C, the critical heat flux (CHF), heat flux decreases in the boiling curve. This can be explained by a vapor film covering the heated surface, leading to a large thermal resistance. Film boiling starts at point D, Leidenfrost point, where the surface is fully covered by a vapor film. In this region, thermal radiation plays a critical role to increase the heat transfer rate between water and surfaces due to the large surface temperature.

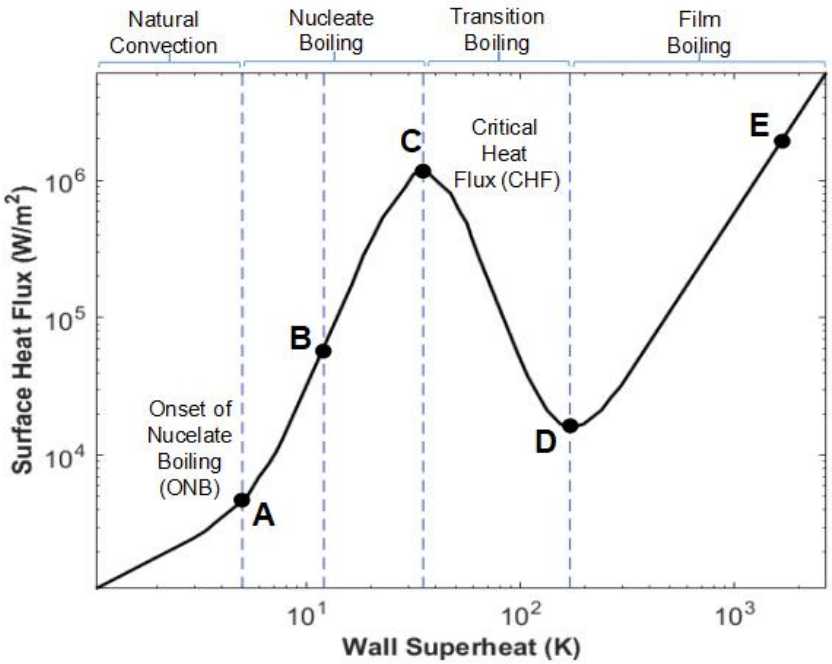

Figure 1-1. Typical boiling curve, from Nukiyama [1]. It expresses the boiling heat transfer characteristics for varying wall superheat.

Compared to traditional conduction and convection cooling methods, nucleate boiling heat transfer achieves much higher heat fluxes. In the past decades, many researchers have explored the boiling characteristics as well as the heat transfer mechanisms. One of the most accepted theorem for nucleate boiling inception was proposed by Hsu [3], which explains that vapor bubble starts to grow if the embryo (gas-filled cavity) reaches the saturation temperature at the tip (the farthest point from the heated wall). Apart from this popular theory, boiling inception was also reported to be a result of the instabilities of the liquid-vapor interface (Mizukami [4] and Forest [5]). Boiling heat transfer is dominated by the combination of transient conduction, microlayer evaporation, and phase change in superheated liquid layer. Heat transfer signatures for each of the above mechanisms are quite distinct, and each of them may dominate in different boiling conditions. The model of transient conduction was proposed by Han and Griffith [6] in 1962. As shown in figure 1-2 (a)-(d), bubbles departing from the heated wall scavenge away the superheated layer surrounding the bubble over an area twice the bubble departure diameter, where the cold bulk liquid fills this area at the same time.

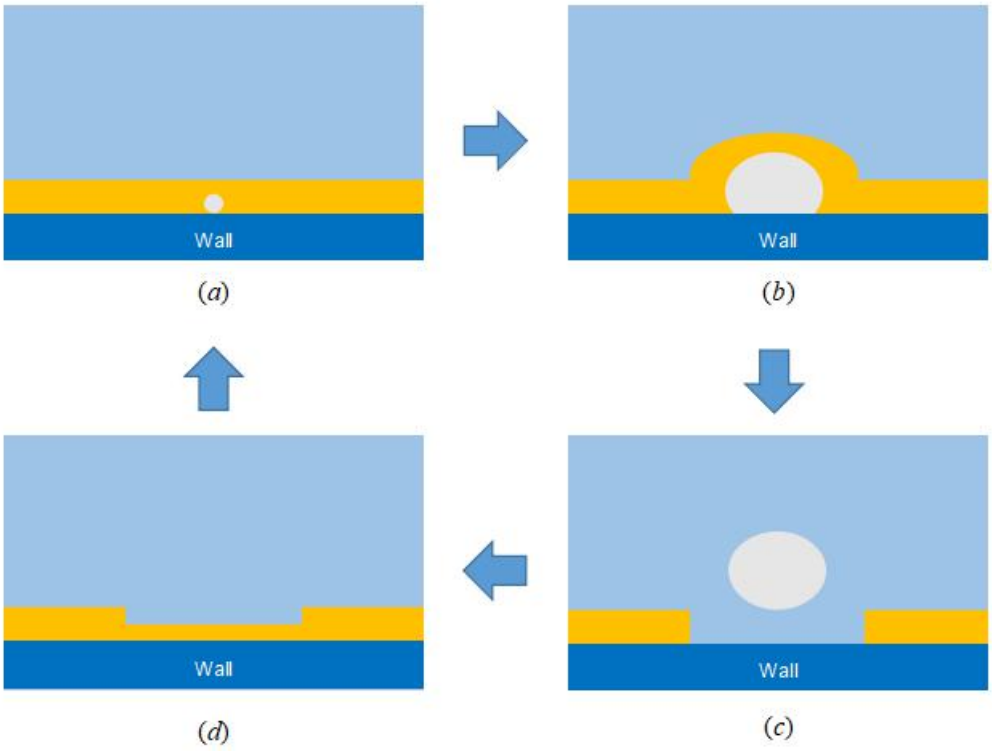

Figure 1-2. Transient heat conduction model, from Han and Griffith [6]: (- bubble; - superheat liquid layer; - water; - wall) (a) bubble nucleation in superheated liquid layer; (b) bubble growth in superheated liquid layer; (c) bubble departure and removal of superheated liquid layer; (d) the growth of new superheated liquid layer. Transient conduction during the waiting time is assumed to be the major heat transfer mechanism.

The transient conduction from a heated wall into colder bulk liquid before the nucleation of a new bubble is assumed to be the dominant heat transfer mode. The superheated liquid layer above the heated wall is reformed during the waiting time (the period of time between bubble departure and the nucleation of a new bubble). Based on the work of Han and Griffith [6], Mikic and Rohsenhow [7] developed a bubble growth model based on the transient conduction theory.

Snyder and Edwards [8] suggested that growing bubble would trap a micron scale liquid layer between bubble base and heated wall based on their experiment results. In order to further understand the characteristics of microlayer in different boiling conditions, Cooper and Lloyd [9] observed a temperature fluctuation during the boiling of toluene and

isopropyl alcohol on glass and ceramic substrates. Based on their experimental results, they argued that the thickness of the initial microlayer obeys the following equation:

$$\delta_0 = C_2\sqrt{\nu_l t_g} \tag{1}$$

where C_2 is a constant of order 0.8, ν_l is the liquid kinematic viscosity and t_g is the time taken for the bubble diameter increasing to a characteristic length. Based on the aforementioned microlayer evaporation theorem, Voutsinos and Judd [10] found out that the thickness of microlayer is in the range of 1-6 μm according to their dichloromethane boiling test. They also noticed that the microlayer thickness increases with distance from the bubble nucleation site. Based on their theory, the wedge-shaped microlayer underneath a vapor bubble is shown in figure 1-3 (a). Koffman and Plesset [11] executed subcooled pool boiling experiments for both water and ethanol. They captured the distributions of microlayer thicknesses through a high-speed camera. Christopher [12], Son [13] and Lee [14] numerically modeled the fluid flows and evaporation processes within microlayers using lubrication theory.

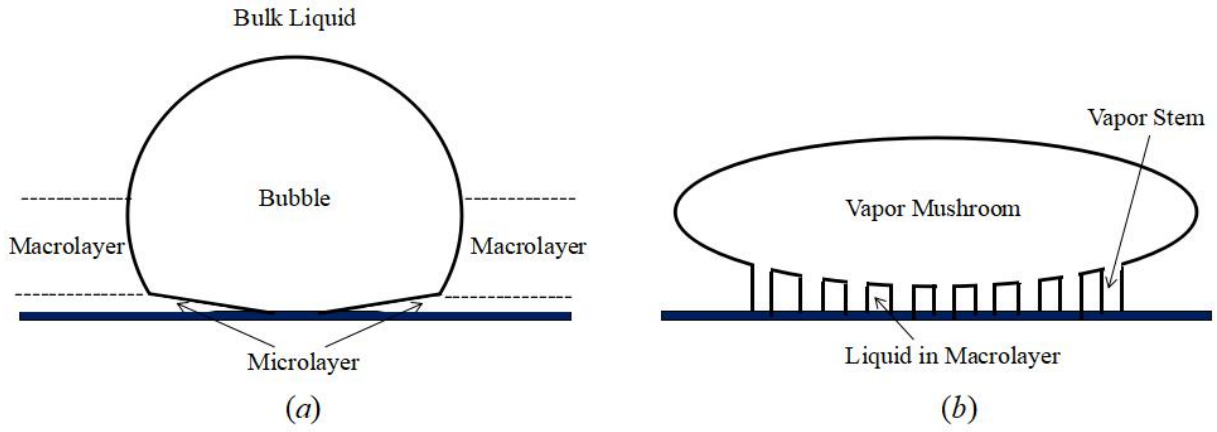

Figure 1-3. Microlayer and macrolayer model: (a) single bubble, from Voutsinos and Judd [10]; (b) bubble mushroom, from Gaenrtner [15]. Microlayer and macrolayer evaporation is important to enhance the boiling heat transfer.

Apart from the transient heat conduction and microlayer evaporation theorem mentioned above, Gaenrtner [15], Sadasivan [16] and Das [17] suggested that phase change processes

and fluid instabilities inside the macrolayer region (figure 1-3 (a) and (b)) also contribute a lot to the high efficiency of boiling heat transfer at both single bubble and bubble mushroom (high heat flux) conditions. Stephan and Hammer [18] considered the evaporation of a thin liquid meniscus at the three-phase contact line as the dominant mode for boiling heat transfer.

Although all kinds of the aforementioned boiling heat transfer mechanisms are valid and clear, the most dominant physics to decide the specific boiling environment is still unrevealed. Kim [19] wrote a comprehensive review including the above-mentioned boiling heat transfer theorems and did experiments to determine the dominant heat transfer mechanism under different boiling conditions. According to his discussion, the dominant boiling heat transfer mechanism for nucleate pool boiling with isolated bubbles might be transient conduction and/or micro-convection. Heat transfer through microlayer evaporation or contact line evaporation does not account for more than approximately 25% of the overall heat transfer and often substantially less. He also argued that a single model incorporating all of the above-mentioned submodels could not be sufficient to describe the total heat transfer performance since each of the above-mentioned mechanisms contributes with varying degrees.

Even though the advantages of boiling heat transfer inspire numerous industrial applications to solve the heat transfer problems, the drawbacks are still unexplored. For pool boiling, once the wall heat flux larger than CHF, thermal radiation will dominate the boiling heat transfer where the wall superheat rises to the order of 10^3 K (point E on figure 1-1). This large temperature is able to burn out the heated wall thus causing serious damages to the boiling system. In order to avoid the boiling crisis, applications for boiling heat transfer are mainly limited to nucleate boiling regime before CHF point. In the past decades, numerous scholars have studied the enhancement methods for nucleate boiling heat transfer. One effective way to achieve a higher pool boiling heat flux is through modifying the characteristics of the heated wall. Wang [20] conducted pool boiling experiments with different surface contact angles and discovered that the fraction of the

active cavities decreases as the wettability of the surface improves. Takata [21] obtained an excellent heat transfer characteristic and higher CHF from a TiO_2 coated superhydrophilic heating surface. Jaikumar [22] and Kandlikar [23] designed the surface in the shape of the sintered fin (figure 1-4 (a) and (b)), contour fin (figure 1-4 (c)) and feeder channels in order to separate the pathways of liquid and bubbly flow using evaporation momentum force. During the nucleate boiling process, the incoming liquid acts as an impinging pump and flows towards the nucleation sites, the existing bubbles then slide along or sweep over on a prescribed flow path on the heated surface. Since bubble departure has no interruption on the incoming liquid flow towards the nucleation site, the nucleate boiling process continues uninterrupted to very high heat fluxes with significant enhancements in CHF as shown in figure 1-4 (d).

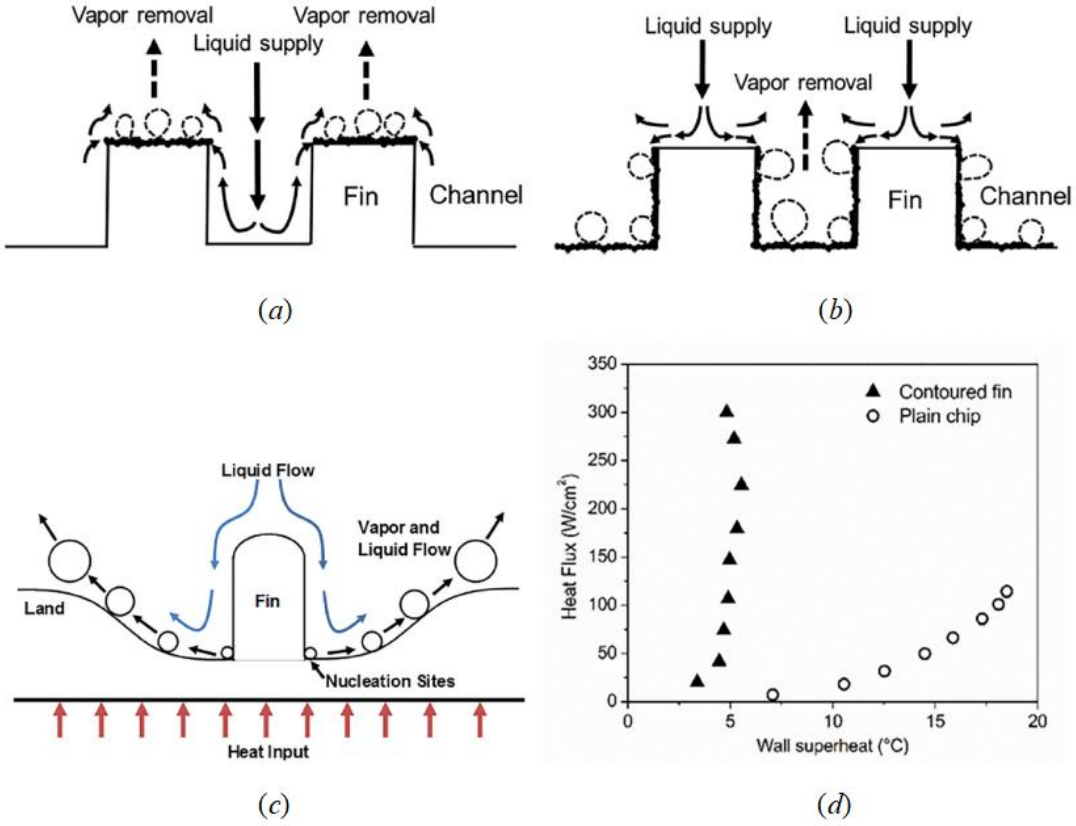

Figure 1-4. Enhanced macroconvection mechanism with separate liquid–vapor pathways, from Kandlikar [25]: (a) sintered fin tops; (b) sintered channels; (c) contoured fin geometry; (d) boiling curve with water at 1atm. Wall heat fluxes are enhanced through the management of liquid-vapor pathways.

Compared to pool boiling, two-phase boiling flow in microchannels has been an efficient method with low thermal resistances and pumping power requirements [24]. However several drawbacks make flow boiling heat transfer less attractive at present. These drawbacks include flow instabilities [25], high peak pressure drops [26][27], and dry-out. For microchannel flow boiling with high heat flux, small vapor bubbles are more likely to merge into a vapor slug, which will block the channel flow and significantly increase the pressure drop. To resolve this issue, the use of locally venting membrane in the two-phase system was proposed by Zhou [28]. Based on this propose work, David [29] developed a copper vapor - venting microchannel with integrated PTFE membranes as illustrated in figure 1-5. In 1981, Inada [30] [31] discovered microbubble emission boiling (MEB) phenomena in the cases of subcooled boiling when large numbers of small bubbles emitted from the coalesced bubble on the heated surface. Compared to the traditional boiling heat transfer, MEB has a much higher heat flux than CHF before the transition boiling starts. This makes MEB become an attractive research with the aim of solving the flow boiling drawbacks. Followed by Inada's work [30] [31], Suzuki [32-34], Kumagai [35] and Tang [36] probed the mechanisms of MEB as well as its applications to industry. However, due to the high flow instability and bubble frequency, its formation mechanism has not been clearly illustrated by far.

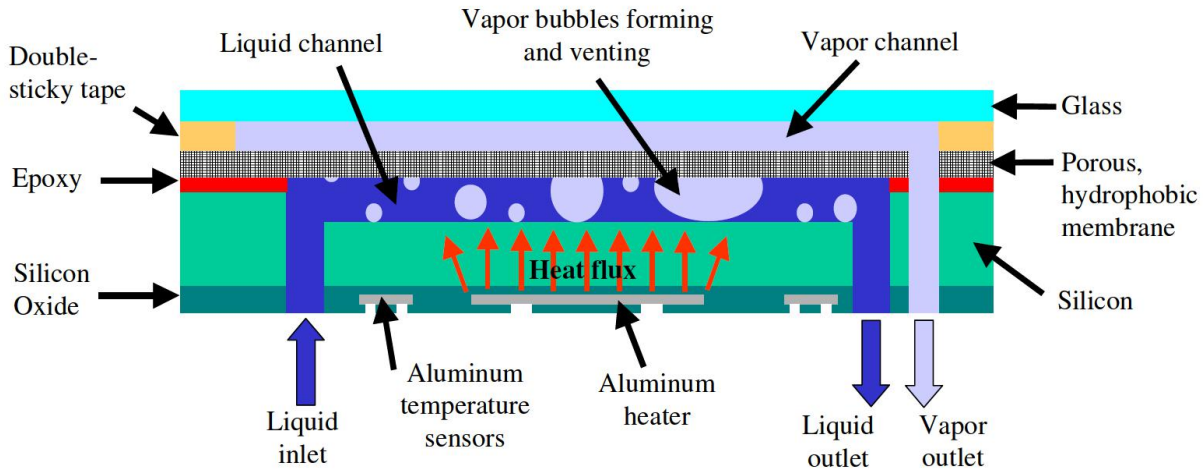

Figure 1-5. Schematic of the vapor-venting microchannel, from David [29]. The pressure drop is effectively reduced by applying a porous membrane at the microchannel top.

Nowadays, with the rapid development of computer science and technologies, computational fluid dynamics (CFD) has become a powerful tool to understand boiling heat transfer as well as multi-phase flow problems. Recent years researchers [37-41] have modeled the boiling process and bubble dynamics with the help of commercial CFD software. Interface tracking and interface fluxes modeling are two major challenges for numerical studies of multi-phase flow with phase interactions. Volume of fluid (VOF) and level set (LS) are two of the most popular methods to capture the interfaces between individual phases. VOF model requires less calculation time but creates an interface jump (discontinuity) between cells. Comparing to VOF, LS is able to obtain a much smoother interface capturing, but it may cause errors during interface curvature calculations as well as serious mass conservation problems [42]. For interface fluxes modeling, Rankine-Hugoniot jump condition [43] is widely used to calculate the net energy transfer across the interface. Schrage [44] used gas kinetic theory to propose a mass transfer model based on the Clausius–Clapeyron relation and Hertz-Knudsen formula. Lee [45] simplified the Schrage model [44] and proposed a widely-used heat and mass transfer model includes an empirical mass transfer coefficient.

Chapter 2. Numerical Methods

Numerical modeling of single bubble behaviors on both flat and pillar heating surfaces is performed in two 8mm × 22mm axisymmetric domains, respectively, as shown in figure 3-1 (a) and (b). Numerical solutions for bubble behaviors are processed through commercial software ANSYS Fluent v18.1.

2.1 Mathematical Models

2.1.1 VOF Model

Bubble interface is tracked by the volume of fluid (VOF) method with piecewise linear interface calculation (PLIC). The VOF model is a fixed-grid technique designed for two or more immiscible fluids [46]. This model solves a coupled momentum and energy equation for the mixture phase and volume fraction for each fluid is calculated within each finite element. Therefore, it is able to track the interface between two phases everywhere in the flow domain. As indicated in the *Introduction*, the major drawback for VOF method coupled with PLIC is unable to obtain a continuous interface. However, this method is much easier and faster to convergent compared with level set and dynamic mesh methods. Interface tracking is accomplished by the solution of a transport equation for the volume fraction of one of the phases. This equation has the following form for incompressible fluids:

$$\frac{\partial \alpha_v}{\partial t} + \nabla \cdot \left(\vec{u} \alpha_v \right) = S_{\alpha_v} \tag{2}$$

where $\vec{u}$ is the fluid velocity vector and S_{α_v} is the source term. α_v represents the volume fraction of vapor phase in a certain cell whose value is between 0 and 1:

- $\alpha_v = 0$ no vapor phase inside the cell
- $\alpha_v = 1$ only vapor phase inside the cell
- $0 < \alpha_v < 1$ the cell is filled with both liquid and vapor phase

In water-vapor two-phase flow, the summation of volume fraction for each phase is equal to 1.

$$\alpha_v + \alpha_l = 1 \tag{3}$$

Mass conservation (continuity) equation for vapor phase based on VOF model can be expressed as follows:

$$\frac{\partial(\alpha_v \rho_v)}{\partial t} + \nabla \cdot (\alpha_v \rho_v \vec{u}) = \dot{m}_{lv} - \dot{m}_{vl} \tag{4}$$

$\dot{m}_{lv}$ represents the mass transfer rate (kg/m^2·s) from liquid to vapor phase. The liquid phase mass conservation equation can be obtained by reversing the subscript *v* and *l* from equation (4). Unlike Euler model which solves the momentum (Navier-Stokes) and energy equations respectively for each phase, VOF model couples separate momentum as well as energy equations with volume-fraction-averaged properties. The averaged density is defined as equation (5), other parameters such as internal energy, viscosity, and thermal conductivity are averaged through equation (6) where ϕ represents any of the aforementioned properties. Solving for the coupled momentum and energy conservation equations (equation (7) and (8)) are able to reduce a large amount of calculation time.

$$\rho = \alpha_v \rho_v + \alpha_l \rho_l \tag{5}$$

$$\phi = \frac{\alpha_v \rho_v \phi_v + \alpha_l \rho_l \phi_l}{\alpha_v \rho_v + \alpha_l \rho_l} \tag{6}$$

$$\frac{\partial(\rho \vec{u})}{\partial t} + \nabla \cdot (\rho \vec{u} \vec{u}) = \nabla P + \nabla \left[\mu \left(\nabla \vec{u} + \nabla \vec{u}^T \right) \right] + \rho \vec{g} + \vec{F} \tag{7}$$

$$\frac{\partial(\rho E)}{\partial t} + \nabla \cdot \left[\vec{u} (\rho E + P) \right] = \nabla \cdot \left(k_{eff} \nabla T \right) + S_h \tag{8}$$

k_{eff} in equation (8) refers to the effective thermal conductivity calculated from equation (6), and S_h is the energy source term. Here we should note that the energy diffusion and dissipation caused by fluid viscosity is assumed to be negligible by ANSYS Fluent. This means extra calculation error will be produced if the vapor flow is highly compressible.

2.1.2 Phase Change Model

Lee evaporation-condensation model [45] has been employed to express the heat and mass transfer process across bubble interface. Based on Lee model, the mass source term ($\dot{m}_{lv}$, $\dot{m}_{vl}$) as well as the energy source term (S_h), are defined by equation (9-10) and (11-12), respectively. The model assumes that the mass is transferred at constant pressure and quasi-thermo-equilibrium state [42] according to the following relations:

$$\dot{m}_{lv} = r\alpha_l\rho_l\frac{(T - T_{sat})}{T_{sat}} \quad \text{for evaporation } (T > T_{sat}) \tag{9}$$

$$\dot{m}_{vl} = r\alpha_v\rho_v\frac{(T_{sat} - T)}{T_{sat}} \quad \text{for condensation } (T < T_{sat}) \tag{10}$$

The corresponding energy source term is defined as follows:

$$S_h = -\dot{m}_{lv}\cdot h_{fg} \quad \text{for evaporation } (T > T_{sat}) \tag{11}$$

$$S_h = \dot{m}_{vl}\cdot h_{fg} \quad \text{for condensation } (T < T_{sat}) \tag{12}$$

where h_{fg} is the latent heat, which is set to be a constant (2,257,600J/kg). T_{sat} refers to the saturation temperature for water under an atmospheric pressure. r is an empirical coefficient called mass transfer intensity factor and has the units of s^{-1}. In order to maintain a small temperature difference on both sides of the bubble interface, values of r recommended by researchers are in a large range from 0.1 to 10^7 s^{-1}. In early studies, the value of 0.1s^{-1} had been widely used [47-48]. Later the 100 s^{-1} was used for flow boiling simulations [24] [49]. In most recent researches large values of r from 10,000 s^{-1} [50] to 10^7 s^{-1} [51] have been reported to be valid in micro-scale phase change phenomena. A key challenge for applying the Lee model is that different r values have been recommended by different researchers for similar experimental configurations, depending on the specific setup of a numerical model used [42]. This implies that r should be allowed to vary throughout the whole domain as to increase the solution accuracy [50]. In the present study, the value of r = 1000s^{-1} is selected considering both numerical accuracy and convergent speed.

2.1.3 Density Variation

To model the natural convection during pool boiling, the liquid density is set to be a function of temperature. Boussinesq approximation is applied to modify the density variation (equation (14)) based on thermal expansion coefficient (equation (13)).

$$\beta = -\frac{1}{\rho}\left(\frac{\partial \rho}{\partial T}\right)_P \tag{13}$$

$$\rho = \rho_0\left(1-\beta\right)\left(T - T_{sat}\right) \tag{14}$$

where ρ_0 is the density of liquid water at saturation point (960kg/m^3). The Boussinesq approximation is valid only when $\beta\left(T - T_{sat}\right) << 1$.

2.3.4 Surface Tension

Surface tension is an important factor that impacts both bubble growth and departure. Continuum surface force (CSF) model [52] is used to transfer the surface tension force into a body force, which can be plugged into the momentum source term $\vec{F}$ in equation (7). The full expression for CSF model is defined as:

$$\vec{F}_{vol} = \sum_{ij, i<j} \sigma_{ij} \frac{\alpha_i \rho_i \kappa_j \nabla \alpha_j + \alpha_j \rho_j \kappa_i \nabla \alpha_i}{1/2 \cdot \left(\rho_i + \rho_j\right)} \tag{15}$$

where subscripts *i* and *j* refer to the index of two identical phases, σ_{ij} means the surface tension coefficient between phase *i* and *j*, respectively, and κ is the surface curvature. For cases where two phases contained in a cell, $\kappa_i = -\kappa_j$ and $\nabla \alpha_i = -\nabla \alpha_j$. The above equation can be simplified as:

$$\vec{F}_{vol} = \sigma \frac{\rho \kappa \nabla \alpha}{1/2\left(\rho_l + \rho_v\right)} \tag{16}$$

where ρ is the volume fraction averaged density calculated from equation (5). Interface curvature κ is defined in terms of the divergence of the unit normal vector $\hat{n}$, which is the volume fraction gradient over its norm:

$$\kappa = \nabla \cdot \hat{n} \tag{17}$$

$$\hat{n} = \frac{\nabla \alpha}{\|\nabla \alpha\|} \tag{18}$$

A piecewise - linear method is used to describe the variation of surface tension coefficient σ as a function of temperature. Three specific values of σ are defined from Vargaftik [53], which is shown in table 2-1.

Table 2-1. Specific surface tension coefficient values, from Vargaftik [53].

Temperature (K)	373	378	383
σ (N/m)	0.05891	0.05794	0.05696

2.1.5 Solution Methods

The pressure staggering option (PRESTO) [54] is used for pressure discretization. The second order upwind scheme is adopted for both momentum and energy. Least square cell-based method is used for gradient discretization and volume fraction is geo-reconstructed. For algorithm method, the semi-implicit method for pressure-linked equations (SIMPLE) [54] is used to tackle the velocity - pressure coupling. The basic sequence of steps followed by the SIMPLE algorithm is:

·Set up the boundary conditions

·Guess the pressure field P^* at all grid nodes

·Solve the discretized momentum equation for the velocity field $\vec{u}$

·Get the pressure correction P' to satisfy the continuity equation

·Get the new pressure field $P = P^{*}+P'$

·Get the velocity field $\vec{u}$ based on the new pressure field

·Solve functional differential equations for other properties (enthalpy, temperature, ...)

·Calculate fluid properties such as ρ and C_P based on new *T*'s and *P*'s

·Use the newly calculated P as a starred quantity for the new iteration and repeat the above steps until $P' \Rightarrow 0$

Time step is determined by the definition of global Courant number *Co*:

$$C_O = \frac{\vec{u}\Delta t}{\Delta c} \tag{19}$$

Courant number reflects the relationship between time step and cell size. Generally, *Co* should be no larger than 1 because large *Co* will reduce the calculation stability even though it could effectively speed up the calculation rate. The value of *Co* is selected to be 0.1 in order to improve transient solution's convergence.

2.2 Boundary Conditions

As shown in figure 3-1, the bottom surface is heated, which is non - slip with a constant surface temperature 383K. The left boundary in the axial direction refers to the axis. Both top and right boundaries are set to be pressure outlet. The pressure and backflow temperature at the top surface are defined as constant values 101395 Pa (1 atm) and 373K (saturation temperature) respectively. The pressure at the right outlet is determined by the height in the axial direction to account for the gravity:

$$P(y) = P_a + \rho_l g(H - y) \tag{20}$$

where *Pa* is the atmospheric pressure, *y* is the height in the axial direction, and *H* is the domain height. Gravitational acceleration *g* is in the negative axial direction with the value of 9.81kg/m·s^2. Backflow temperature at this surface is also set to be 373K.

2.3 Initial Settings

In order to model the bubble dynamics using VOF method, the nucleation process cannot be accomplished because a small amount of vapor phase has to be specified at the initial of the computation [39] [57]. Thus, a small vapor bubble is patched at the corner between heated wall and axis (figure 2-1). According to Han [6], the size of nucleation vapor embryo is closely related to thermal boundary layer formation, and the bubble nucleation size is generally much smaller than the boundary layer thickness. In this case, the temperature distribution, as well as the corresponding thermal boundary layer thickness, are calculated. As shown in figure 2-1 and 2-2, the thickness of thermal boundary layer increases while getting closer to the origin (r = 0). An average thermal boundary layer thickness δ_a is calculated as 0.544mm (dash line in figure 2-2), which is defined by the mean thickness for thermal boundary layer from 2mm to 8mm in the radial direction. Initial bubble radius is of the length $r_i = \delta_a / 12$ = 45μm.

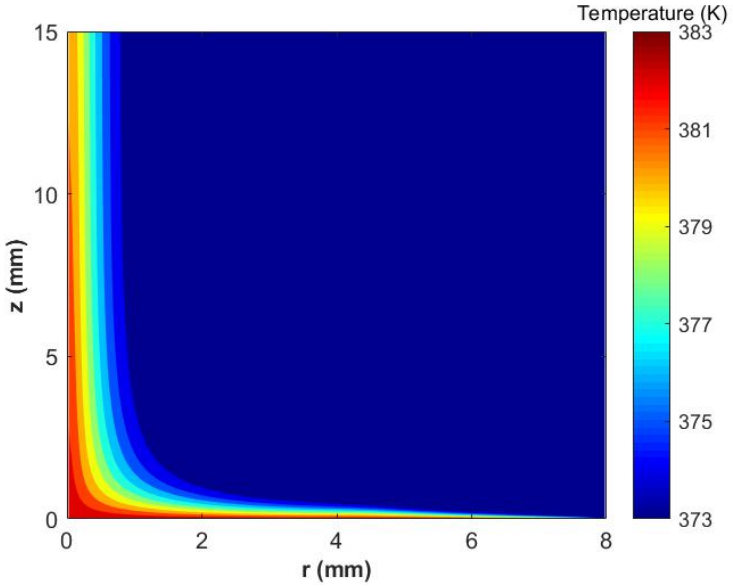

Figure 2-1. Temperature distribution around the wall (r – radial direction; z – axial direction). Heat is transferred through natural convection.

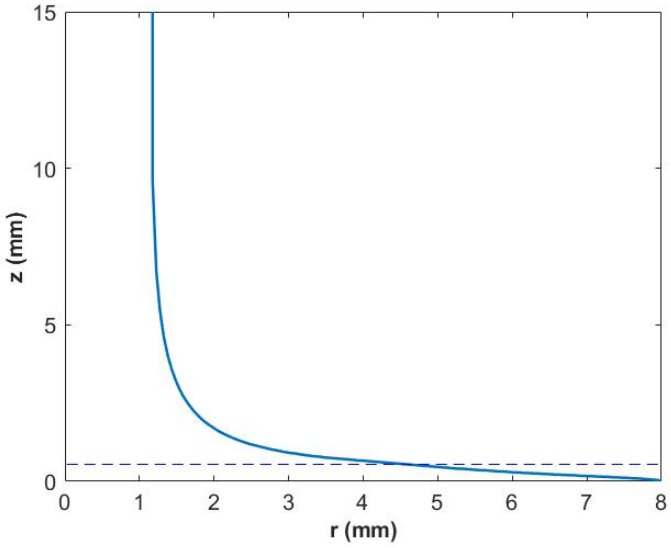

Figure 2-2. Thermal boundary layer thickness (r - radial direction; z - axial direction). The thermal boundary layer thickness is varying in the radial direction.

2.4 Assumptions

Single bubble behaviors under saturated pool boiling conditions are numerically investigated in this paper. In order to simulate them, the heat and mass transfer process achieved by Lee model is applied to the interface meshes to account for the liquid-vapor phase change process. No phase change phenomenon is considered outside the interface region. According to Son [13] and Kim [19], the contribution of microlayer evaporation is less than 25% of the total heat and mass transfer during bubble growth. Therefore the impact of microlayer evaporation is not considered for the phase-change modeling. Pressure profile at the right boundary (equation (20)) and source terms defined by Lee model (equation (9-12)) are employed into Fluent using user-defined function (UDF) macros separately. (See appendix for the UDF details)

Chapter 3. Bubble Behavior Simulation Models

Based on what we discussed in chapter 2, we develop simulation models that can estimate time-dependent bubble behaviors. This chapter will display the numerical results. Commercial software MATLAB and Tecplot are employed for the post-processing.

3.1 Geometry and Boundary Conditions

In order to fully understand the impact of heating surface characteristics to bubble behaviors, we build 2D axisymmetric domains for modeling single bubble behaviors from growth to departure on both flat and pillar heating surfaces. As shown in figure 3-1 (a) and (b), both domains are 8mm in radius and 22mm in height. On flat heating surfaces (figure 3-1 (a)), the influence of contact angle in the range of 72^o to 108^o is studied. Numerical simulations for bubble behaviors on a 1.25mm$\times$2mm pillar are also executed in order to investigate the impacts of the surface structure on the boiling performances. Liquid water and water vapor are employed as the two working fluids, the liquid and vapor properties are listed in table 3-1. As a starting point, a small nucleation embryo with a 45μm radius is patched at the intersection between the axis and the heated wall (section 2.3). Vapor inside the bubble is treated as incompressible whereas the liquid density is a function of temperature (section 2.1.3). The bubble grows on a heated wall with constant temperature (383K) under an atmospheric pressure, where the saturation temperature is set to be 373K.

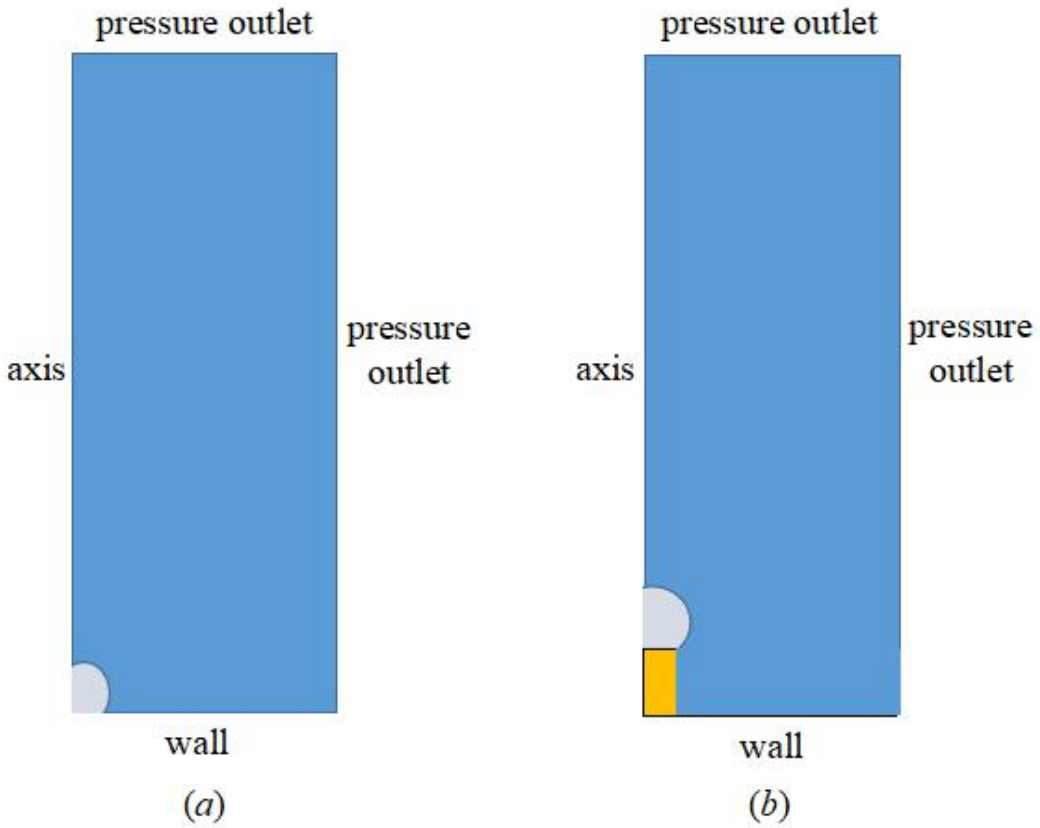

Figure 3-1. Domains for bubble behavior numerical simulation model(■- liquid water; ■- vapor bubble; ■- pillar): (*a*) 8mm×22mm domain with a flat heating surface; (*b*) 8mm×22mm domain with a 1.25mm×2mm pillar on heating surface. 3D bubble behaviors are represented in the 2D axisymmetric domains.

Table 3-1. Fluid properties of the working fluids.

Fluid	Density (kg/m^3)	Specific Heat (J/kg·K)	Thermal Conductivity (W/m·K)	Viscosity (kg/m·s)	Thermal Expansion Coefficient (1/K)
Water	960	4182	0.6	0.001003	0.042
Vapor	0.5891	Piecewise Polynomial	0.0261	1.34e-5	Incompressible

3.2 Mesh Independent Test

In order to test the influence of grid size on the simulation results, three meshes with different size and cell number are tested and compared, the detailed information for each case is shown in table 3-1. The minimum size (minimum length of grid edges) for the three meshes are 10μm, 5μm, and 3.33μm, whereas the cell number for the corresponding cases are 69,300, 135,000, and 175,000, respectively. Grids near the heated wall are refined in order to obtain a more precise bubble dynamic behaviors as well as a more accurate thermal boundary layer distribution.

For the above mentioned three types of meshes, the variation of bubble equivalent diameters with time is shown in figure3-2. Bubble departs around the same diameter for those three meshes whereas the finer mesh will obtain a longer bubble growth period. Wall heat fluxes are also calculated for each case based on equation (24). As shown in figure 3-3, wall heat flux slightly increases with the minimum mesh size. A detailed comparison of bubble departure diameter, bubble period as well as wall heat fluxes between these three meshes are shown in table 3-2. The impact of grid size on simulation results is represented by the difference of wall heat flux. According to table 3-2, the maximum difference for wall heat flux is 6.87%. Therefore, most of the numerical simulations in this study has been performed with the 10μm mesh to minimize the computing costs.

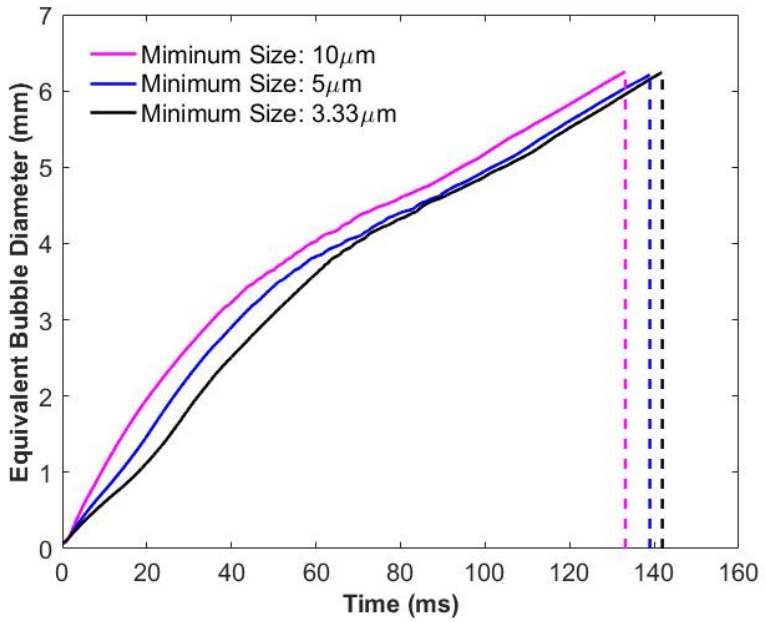

Figure 3-2. Variation of bubble equivalent diameter with time for three different meshes. Close departure diameters with 4.98% - 6.44% deviation for bubble period.

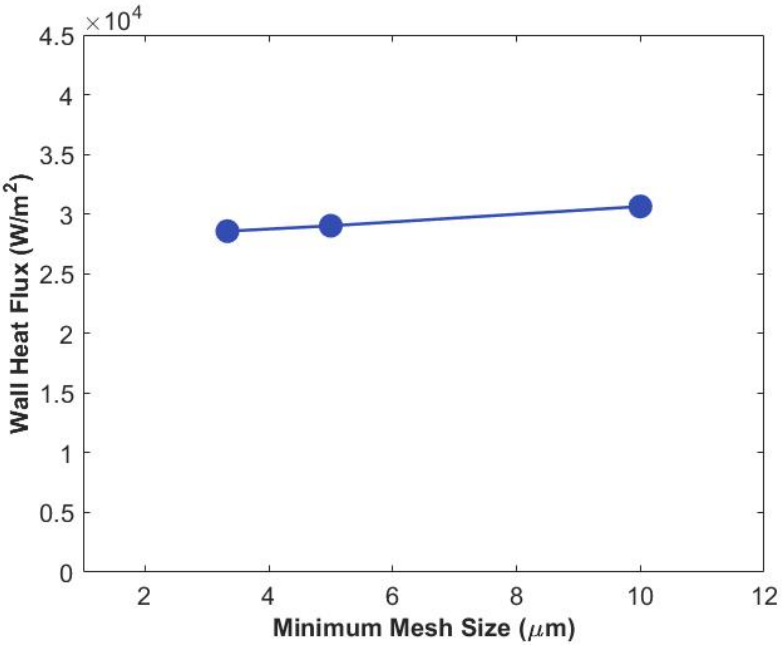

Figure 3-3. Wall heat flux difference created by mesh size. The maximum difference is 6.87%, suggesting the use of mesh size of 10μm to minimize the computing costs.

Table 3-2. Detailed information for mesh independent test.

Mesh Type	Minimum Mesh Size (μm)	Number of Grids	Bubble Departure Diameter (mm)	Bubble Period (ms)	Wall Heat Flux (W/m^2)	Difference for Wall Heat Flux
1	10	69,300	6.092	132.77	30,631	—
2	5	135,000	6.236	139.74	29,015	5.28%
3	3.33	175,000	6.246	141.92	28,526	6.87%

3.3 Bubble Behavior on Flat Surfaces

Bubble behaviors on a 383K heating surface are simulated from growth to departure for varying contact angles 72°, 81°, 90°, 99°, and 108°. In real cases, the contact angles for heating surfaces are dynamic and should be functions of local pressure as well as viscous drags, as indicated by Cho [55] [56]. However, in order to simplify the numerical model and reduce the calculation time, contact angles are treated as constant in this paper. Examples of the numerical results are presented in figure 3-4 (*a*) - (*e*) where the vapor phase is blue color and liquid phase is red. In order to have a clear view of the bubble shape varies with time, figures for bubble behaviors are shown for a 16mm×12mm region above the heated wall. For each case, bubble growth has undergone some similar processes before its departure. Throughout the whole bubble growing period, the bubble shapes will not always maintain a uniform circle. This means that in order to represent the bubble size by a variable in length (such as radius or diameter), we need to use the equivalent bubble diameter D_e derived from bubble volume. Based on the bubble area in the 2D axisymmetric domain, Fluent is able to calculate and report the bubble volume V_v in the corresponding 3D cylinder. Therefore, the time-dependent bubble equivalent diameter D_e is defined as:

$$D_e = 2 \times \sqrt[3]{\frac{3V_v}{4\pi}} \tag{21}$$

As shown in figure 3-5, equivalent diameter D_e increases with a larger speed in the initial stage (before 50ms), which corresponds a semi-spherical bubble shape during this period.

The increment of D_e slows down after the initial stage. Bubble length extends in the axial (vertical) direction accompanied by a shrink in the bubble base. In the final stage (after 100ms), bubble departs from the heating surface, leaving a small amount of vapor attached to the heated wall, which will work for a bubble nucleation site for the next cycle. Contact line diameter (or bubble base diameter) is defined as the diameter of the contact line between bubble base and the heating surface. The variation of contact line diameter as a function of time is presented in figure 3-6. In the initial stage, with the spherical bubble shape, the contact line diameters increase with the similar slope as the corresponding equivalent bubble diameters. After reaching a certain value, all of these contact line diameters will remain that specific length until bubble detaching from the heating surface.

Bubble departure diameter and bubble period are two important factors to express the bubble behaviors as well as the heat transfer performance of the heated wall. Bubble departure diameters are the final or equivalent diameter of the vapor bubble after it departs from the heated surface during boiling [57]. From the simulation models, they are obtained through equation (21) by simply replacing V_v to the volume of vapor detached from the heated wall. Bubble period in this simulation is defined as the period of time for a single bubble growing from the initially patched vapor embryo to its departure. A smaller bubble departure diameter is generally accompanied by a shorter bubble period. A more frequent bubble cycle (from bubble nucleation to its departure) can provide a higher heat transfer efficiency. Surface wettability is an important parameter for the modification of bubble period and its departure diameter in order to enhance the surface heat flux [58]. Therefore, the studies for bubble period as well as departure diameter as a function of the contact angle is of great importance.

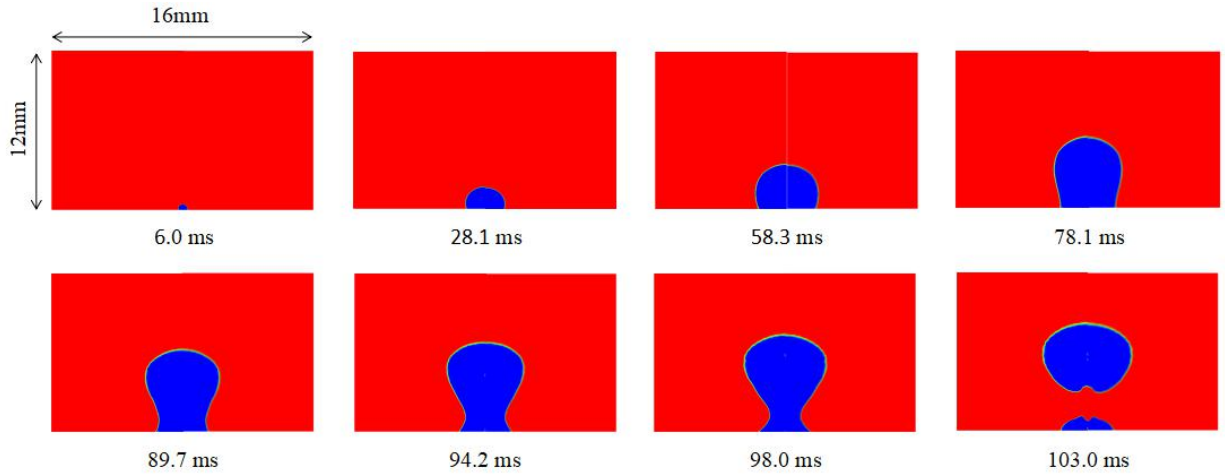
16mm
12mm
6.0 ms
28.1 ms
58.3 ms
78.1 ms
89.7 ms
94.2 ms
98.0 ms
103.0 ms

(*a*)

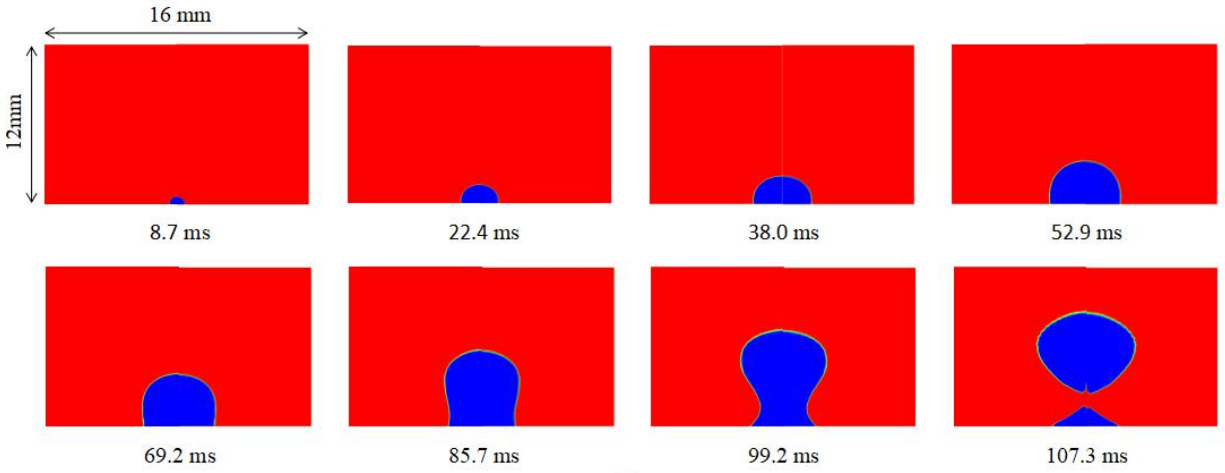
16 mm
12mm
8.7 ms
22.4 ms
38.0 ms
52.9 ms
69.2 ms
85.7 ms
99.2 ms
107.3 ms

(*b*)

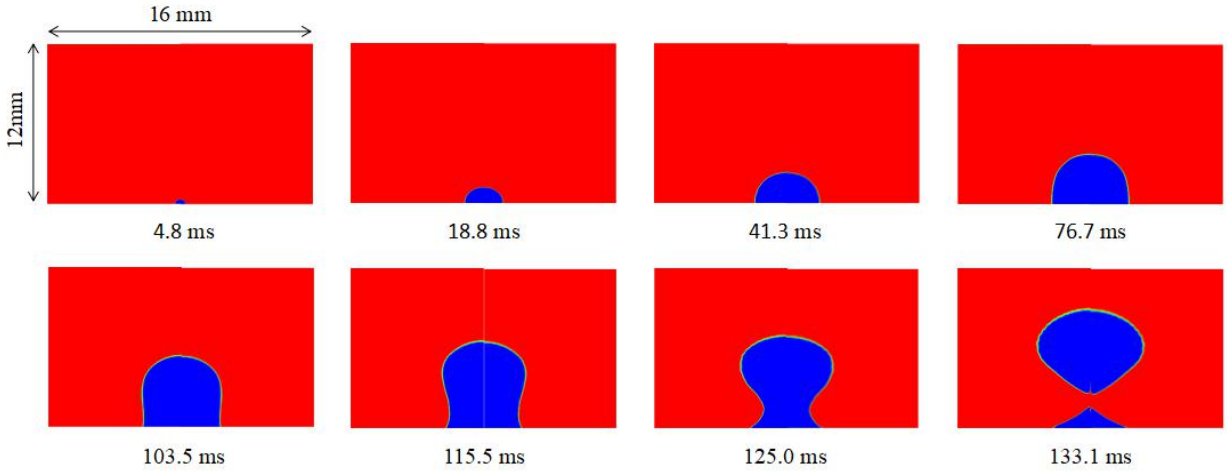
16 mm
12mm
4.8 ms
18.8 ms
41.3 ms
76.7 ms
103.5 ms
115.5 ms
125.0 ms
133.1 ms

(*c*)

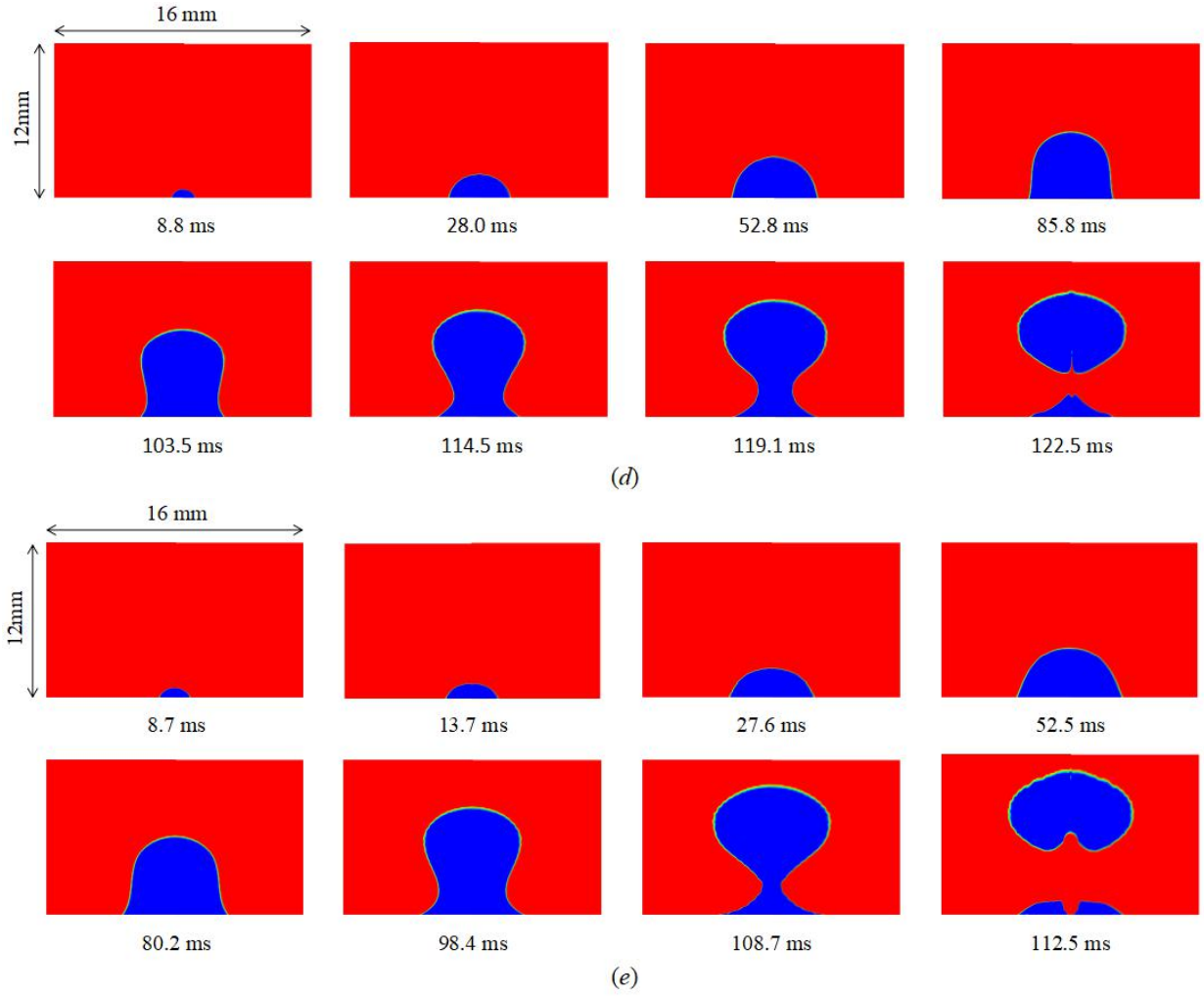

Figure 3-4. Bubble behaviors on flat surfaces with different contact angles (■ - water; ■ - vapor): (a) contact angle = 72°; (b) contact angle = 81°; (c) contact angle = 90°; (d) contact angle = 99°; (e) contact angle = 108°. Similar bubble growth and departure processes with varying departure diameter and bubble period.

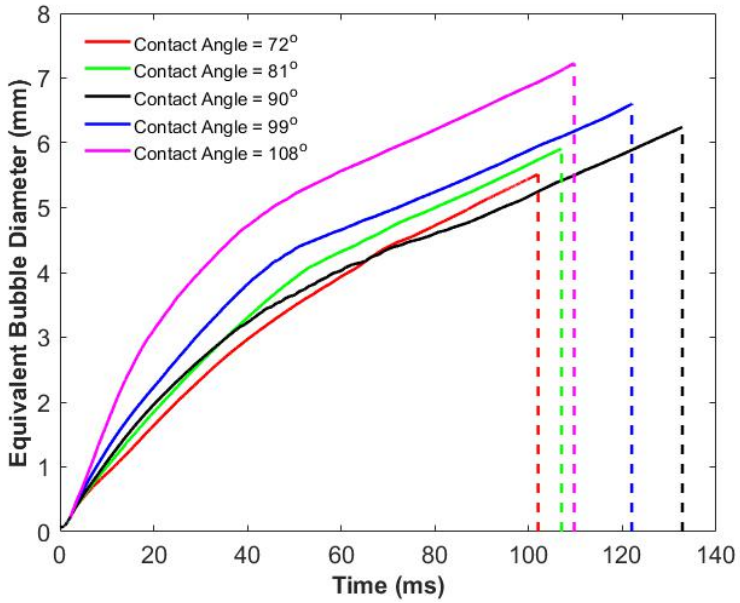

Figure 3-5. Variation of equivalent bubble diameters with time for different surface contact angles. Bubble growth rates decrease after approximate 50ms.

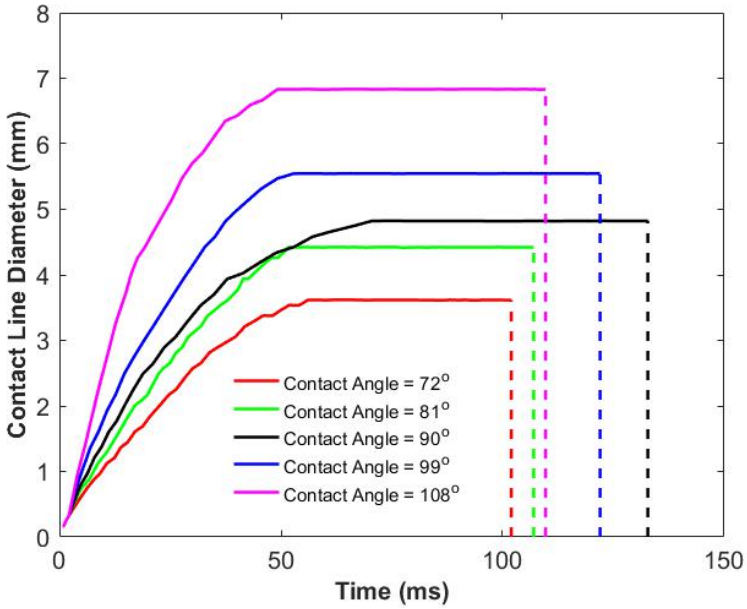

Figure 3-6. Variation of contact line diameters with time for different surface contact angles. Contact line diameters become a constant after approximate 50ms until bubble departure.

Fritz [59] proposed a bubble departure prediction formula in 1935, which has been widely used in numerous studies. He analyzed the bubble departure as a force balance between buoyancy force and surface tension, where buoyancy lifts bubble in the reverse direction of density and surface tension holds it onto the heating surface. The expression for Fritz model is hereafter:

$$D_d = 0.0208\varphi\sqrt{\frac{\sigma}{g(\rho_l - \rho_v)}} \tag{22}$$

We calculated the estimated bubble departure diameters by using equation (22). Figure 3-7 gives a comparison of bubble departure diameter between numerical results by CFD and Fritz model. The corresponding liquid properties in this study are shown in table 3-1. Fritz model explains that bubble departure diameter increases with contact angle φ in a linear manner. This increase means that hydrophobic surfaces work as bubblephilic surfaces, trying to capture bubbles for a long time. The calculated values from two-phase simulation models are larger than those by Fritz model, showing a consistent trend. This may be a result of evaporation process since Fritz model does not take the evaporation momentum forces into the bubble force balance calculation. Apart from this study, the results of bubble departure diameters from other researchers also give a larger value than Fritz's estimation. Liu [60] numerically modeled the bubble growth on a flat surface with contact angle lower than 25^o, their results present a larger departure diameter than the prediction of Fritz. Recently the theoretical model proposed by Matkovic [61] also indicates that bubble detaches with a larger diameter than values calculated from Fritz model. Compared to bubble departure diameters, contact line diameters before departure have much smaller lengths and are more close to the departure diameter calculated from Fritz model. This is consistent with the simulation results from Mukherjee [62].

As indicated by Fritz model and the numerical results, bubble departure diameter increases with contact angle. Since bubble period is inversely proportional to the bubble departure diameter, it is supposed to increase with contact angle, either. However, the variation of bubble period with contact angle does not follow the aforementioned trend in this study.

According to figure 3-8, the bubble period increases with contact angle from 72° to 90°. However, after reaching the maximum value at 90°, the bubble period is reduced for the surfaces with higher contact angles (99° and 108°). This discordance may come from the flow instability around the contact line region. While contact angle is 90°, surface tension has the maximum value in the vertical direction. Large drag force created by the vertical component of surface tension strongly holds the bubble onto the heating surface, which also makes the flow field much stable around the contact line region. The near-bubble velocity distribution and the corresponding velocity vector field at 50ms are shown in figure 3-10 (a)-(e). With a 90° contact angle, a more inactive velocity field appears around the contact line region comparing to other cases. In order to quantify the velocity in the contact line region, a cell-averaged velocity magnitude u_c is defined in this region, which has the following expression:

$$u_c = \frac{\sum_n u_m}{n} \tag{23}$$

where u_m represents the velocity magnitude for a certain cell, and *n* is the cell number of a 0.3mm $\times$ 0.3mm domain inside the contact line region as illustrate in figure 3-9. Figure 3-11 shows the relation between u_c and contact angle. Comparing figure 3.8 and figure 3-11, we note that the bubble period is inversely proportional to the contact line region velocity u_c, which further explains that the flow instability inside the contact line region plays an important role for the bubble period as well as its departure diameter. Moreover, u_c is also closely related to the wall heat flux q''. The heat flux of a wall with constant temperature is defined by Fluent with the following form:

$$q'' = k_f \frac{T_w - T_f}{\Delta n} \tag{24}$$

where k_f and T_f are thermal conductivity and temperature of the fluid around the heated wall, and Δn is the distance between wall surface and the adjacent local fluid cell center. Figure 3-12 shows the wall heat flux of flat heating surfaces with different contact angles.

From figure 3-11 and 3-12, we note that wall heat flux increases with u_c, which explains that the disturbance triggered by the flow field around the contact line region could enhance the local convective heat transfer rates.

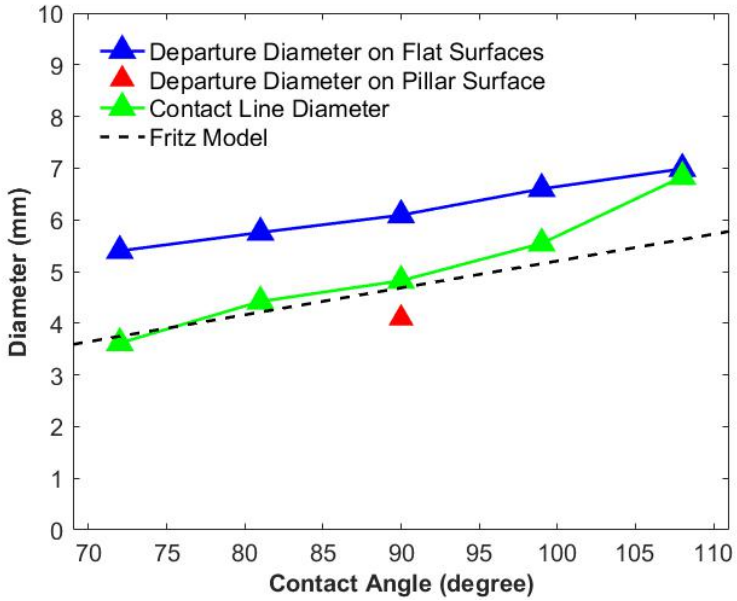

Figure 3-7. Comparison of the bubble departure diameters and contact line diameters with Fritz model. Consistently bubble diameters with Fritz model show large values.

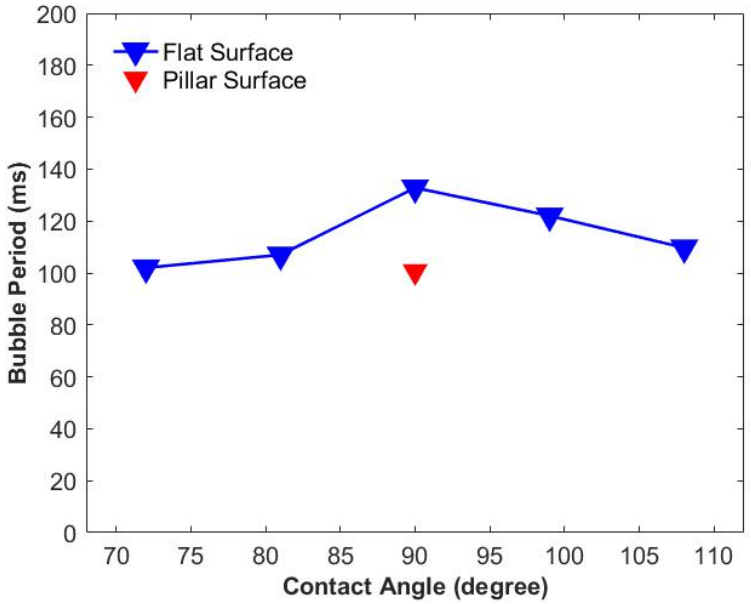

Figure 3-8. Variation of the bubble period as a function of contact angle. The maximum bubble period occurs at 90° contact angle.

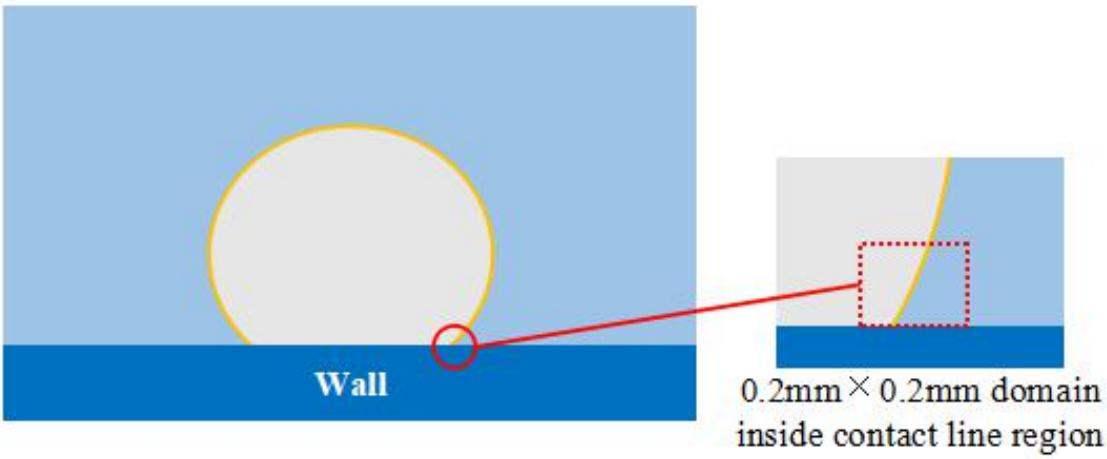

Figure 3-9. Domain for contact line region velocity calculation (- water; - vapor; - wall). Average velocity inside this region is defined as contact line region velocity.

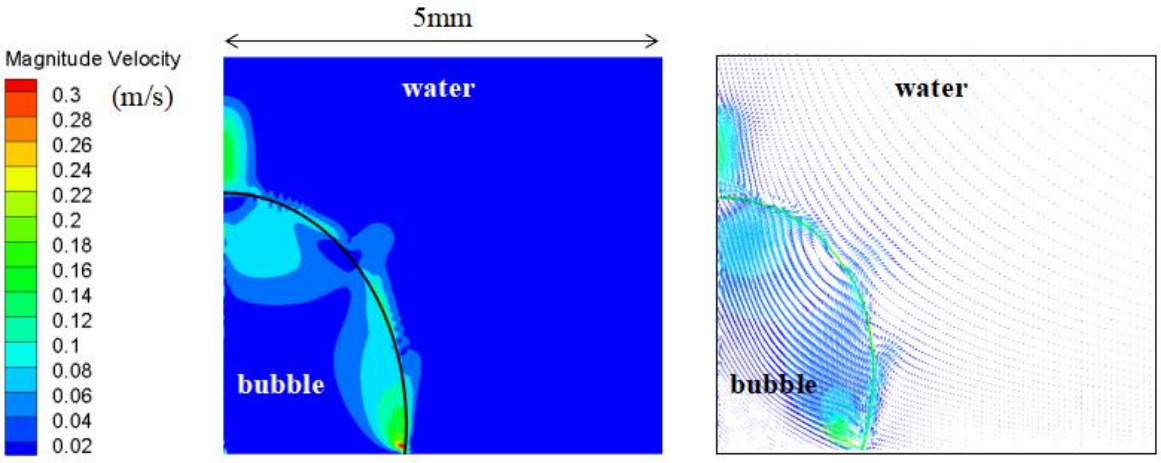

(*a*)

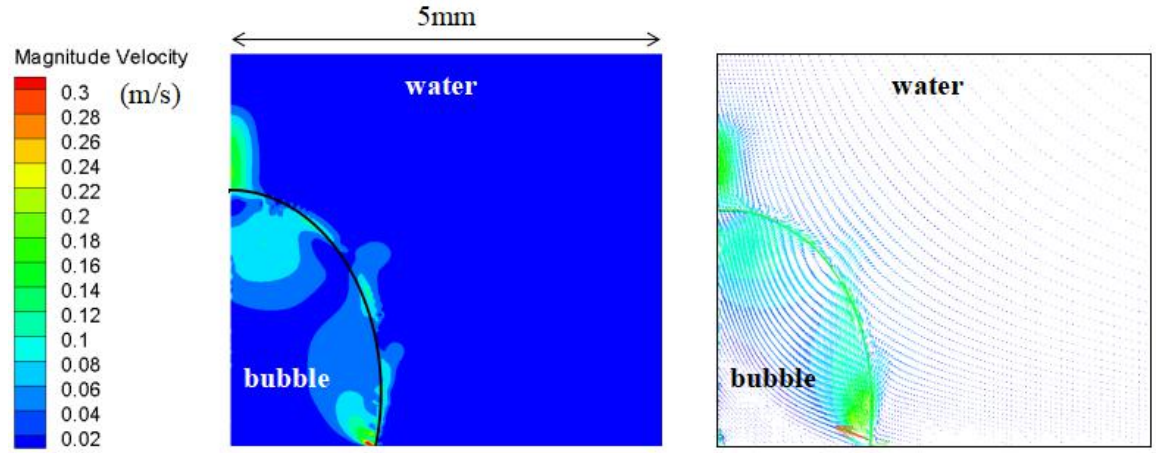
Magnitude Velocity
(m/s)
0.3
0.28
0.26
0.24
0.22
0.2
0.18
0.16
0.14
0.12
0.1
0.08
0.06
0.04
0.02
5mm
water
bubble
water
bubble

(*b*)

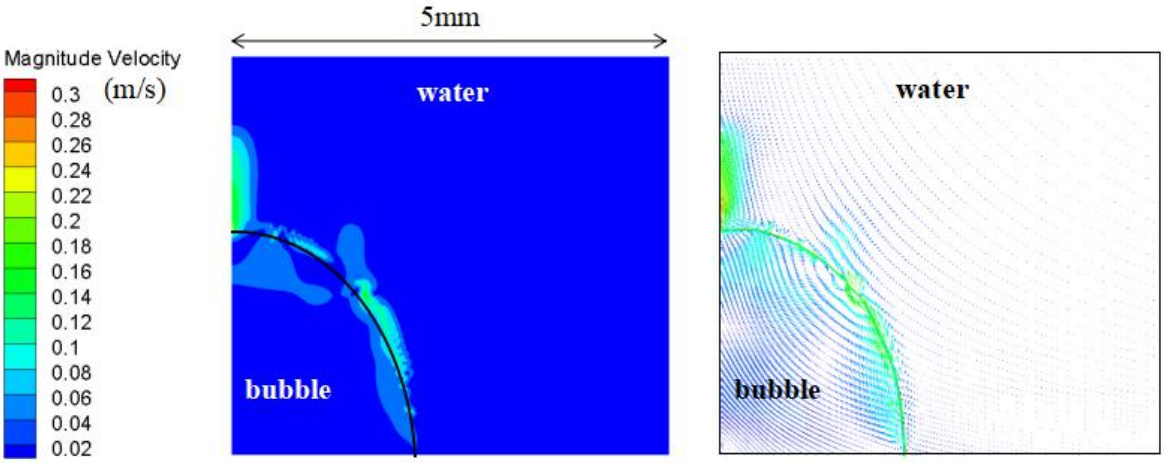
Magnitude Velocity
(m/s)
0.3
0.28
0.26
0.24
0.22
0.2
0.18
0.16
0.14
0.12
0.1
0.08
0.06
0.04
0.02
5mm
water
bubble
water
bubble

(*c*)

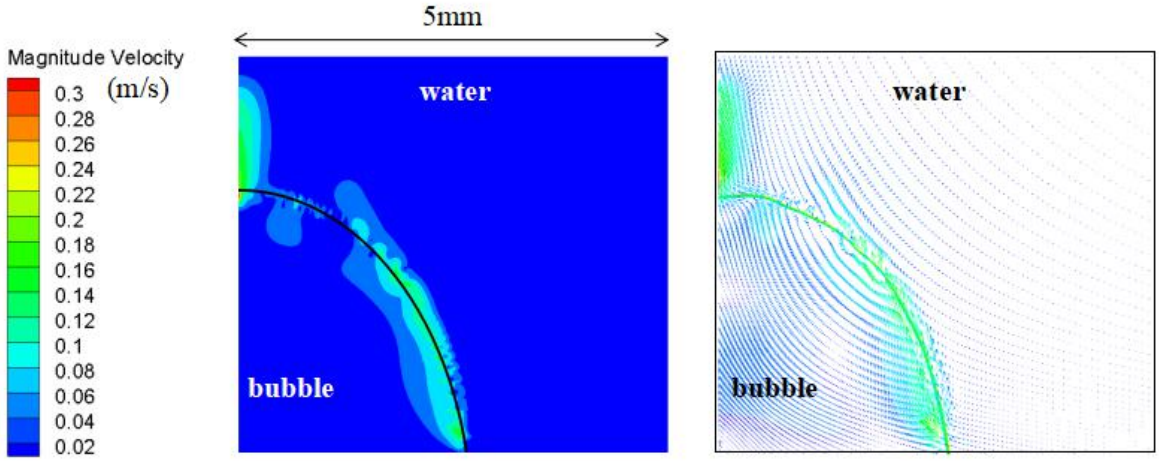
Magnitude Velocity
(m/s)
0.3
0.28
0.26
0.24
0.22
0.2
0.18
0.16
0.14
0.12
0.1
0.08
0.06
0.04
0.02
5mm
water
bubble
water
bubble

(*d*)

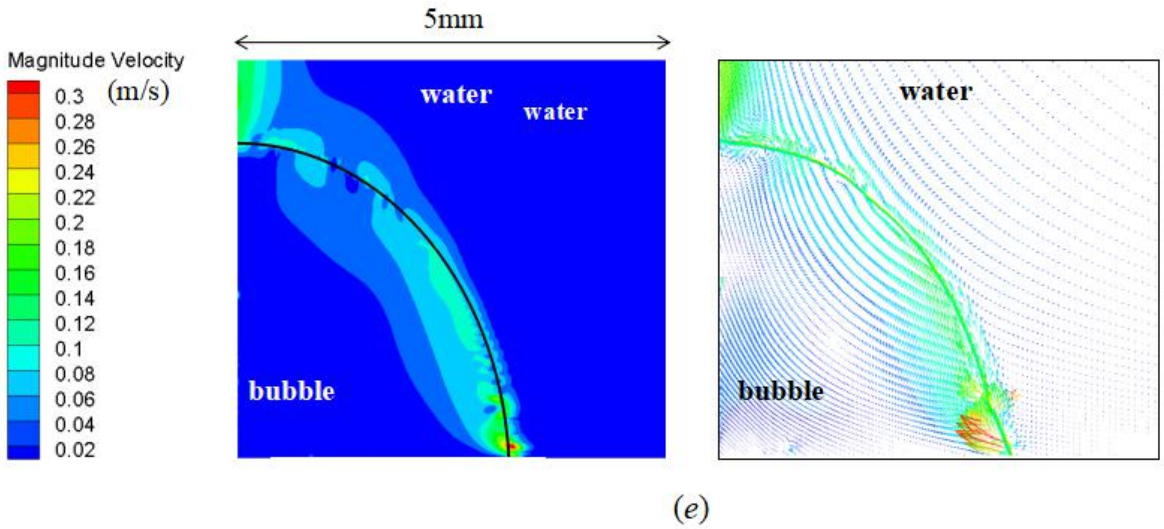

(e)

Figure 3-10. Velocity magnitude and vector field around bubble on flat surfaces at 50ms: (a) contact angle = 72°; (b) contact angle = 81°; (c) contact angle = 90°; (d) contact angle = 99°; (e) contact angle = 108°. Velocity field around bubble interface is most stable while contact angle is 90°.

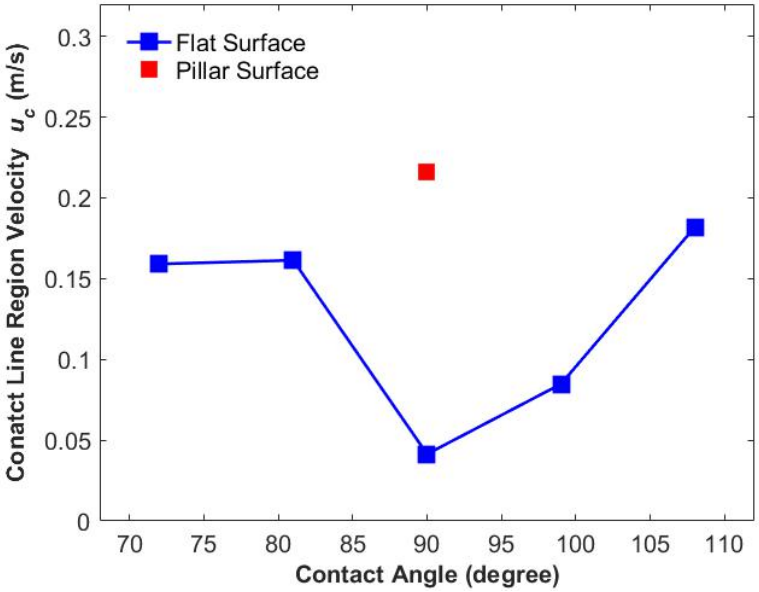

Figure 3-11. Variation of contact line region velocity u_c as a function of contact angle. The minimum contact line region velocity occurs at 90° contact angle.

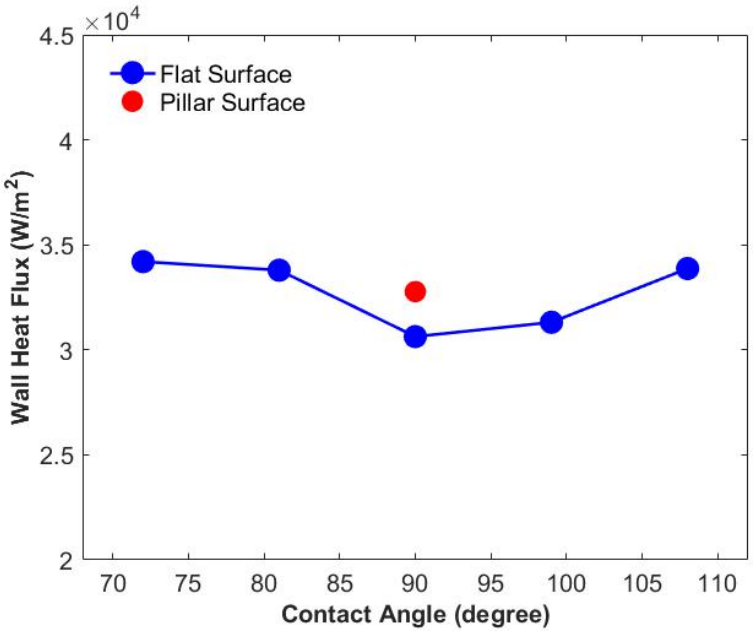

Figure 3-12. Variation of wall heat flux as a function of contact angle. Wall heat flux has the minimum value when the contact angle is 90°.

3.4 Bubble Behaviors on Pillar Surface

As a next step, we model the bubble dynamics on pillar surfaces in order to understand the impacts of structured surfaces on two-phase heat transfer. The bubble evolution on pillar surface from initial embryo to departure is illustrated in figure 3-13, where the pillar is 2mm in height with a 2.5mm diameter. The contact angle for the heated wall is set to be a constant 90°. In this case, the bubble is undergoing similar growing processes as on the flat surface. The comparison between bubble behaviors, detachment diameter, bubble period, and wall heat flux on flat and pillar surface will be presented in next section.

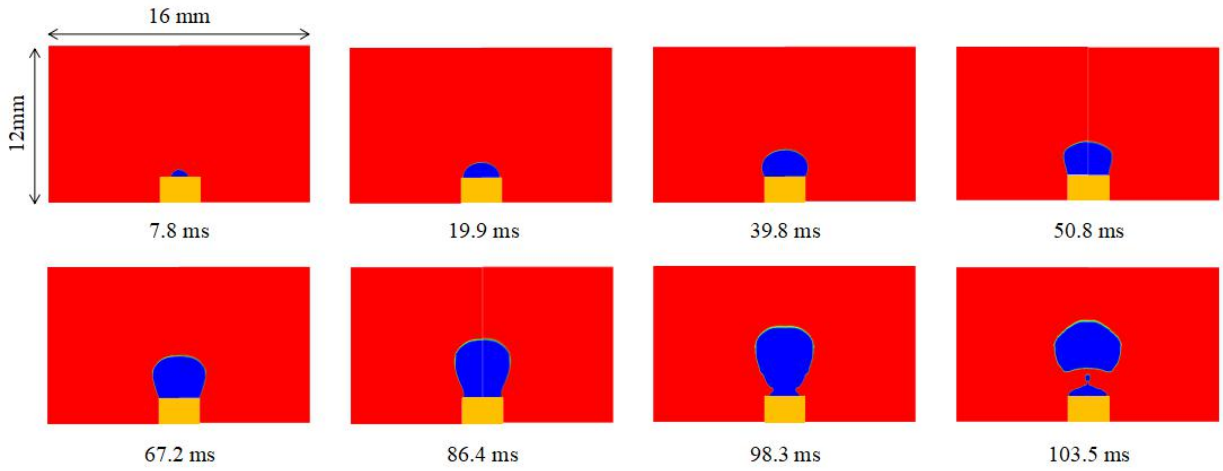

Figure 3-13. Bubble behaviors on pillar surface with a constant contact ang 90°. (water; vapor; - pillar). Bubble growth is constrained in the radial direction.

3.5 Comparison Between Bubble Behaviors on Flat and Pillar Surfaces

Equivalent bubble diameter varies with time on both flat and pillar surface are shown in figure 3-14. At the beginning stage, both vapor embryos start with the same spherical size (45um in radius) and grow with the same speed. Negligible bubble diameter difference presented between those two cases until 20ms, which is the time when the vapor bubble firstly covers the top surface of the pillar. After this point, it is hard for the bubble to continuously grow downwards along the pillar sides because of the enhanced liquid flow along the pillar surface. As explained in figure 3-15, growing bubble tends to expand spherically as a result of the surface tension force on flat heating surfaces. On pillar surface, however, the enhanced near-pillar liquid flow field limits the bubble's expansion in the radial direction and forms it into an oval shape. In this way, the bubble departure diameter, as well as its growth period, are effectively reduced as shown in figure 3-7 and 3-8, respectively.

According to the velocity distribution of the domain with pillar surface (figure 3-16), the near-bubble velocity magnitude is much larger compared to the flat surface case with the same contact angle (figure 3-10 (c)). An active flow field can effectively improve the local

convective heat transfer rate. Therefore, as shown in figure 3-12, the heat flux for pillar heating surface is enhanced by 7%. However, the pillar diameter (2.5mm) should be smaller than the bubble departure diameter on the flat heating surface, otherwise, bubble behaviors and the corresponding heat transfer mechanisms would be less impacted by the pillar structure.

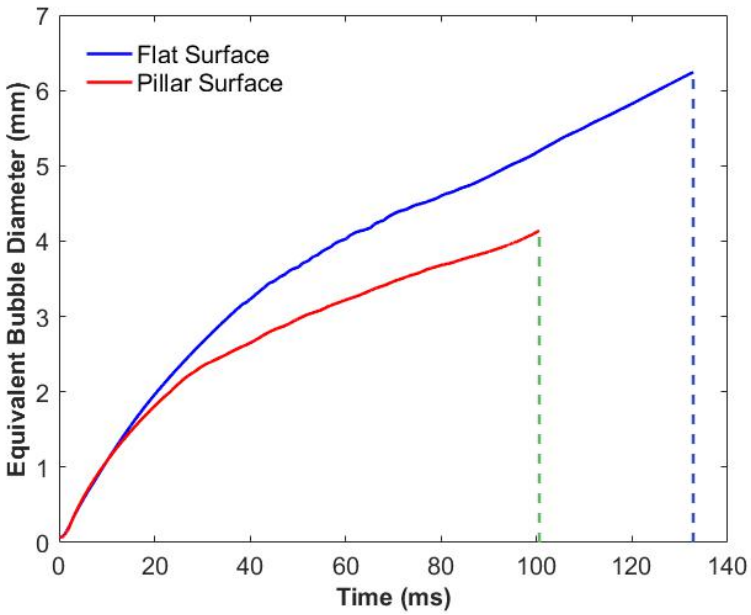

Figure 3-14. Variation of bubble diameter with time on flat and pillar surfaces with a 90 ° contact angle. Both bubble departure diameter and bubble period are reduced while growing on a pillar surface.

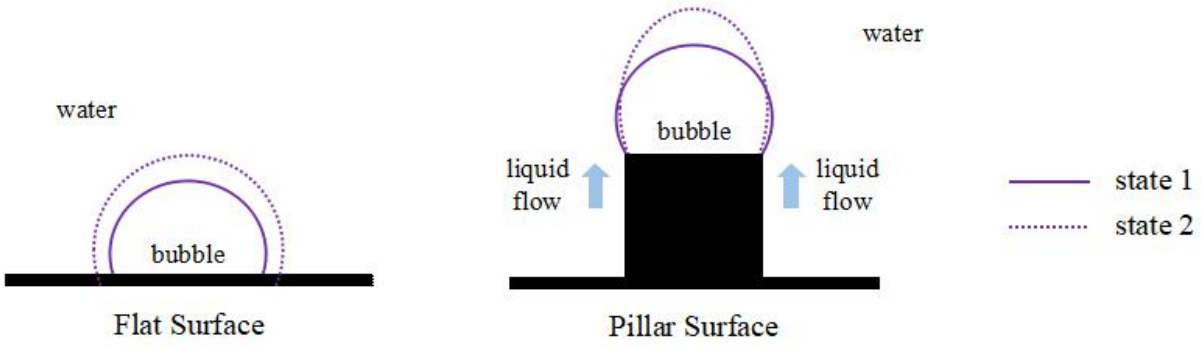

Figure 3-15. Bubble growing from state 1 to state 2 on both flat and pillar surfaces. The near-pillar flow field is responsible for the oval bubble shape on the pillar surface.

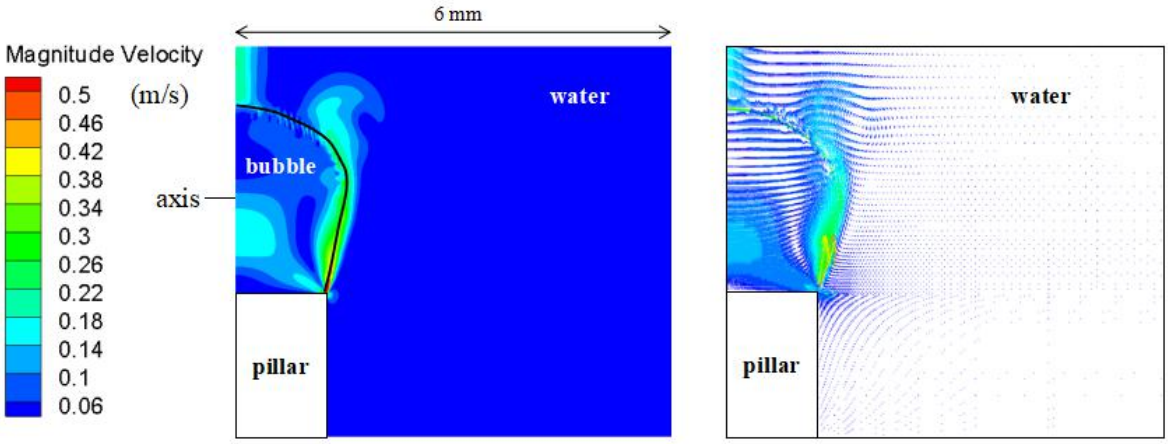

Figure 3-16. Velocity magnitude and vector field around bubble on the pillar surface at 50ms. The velocity field is more active than on the flat surface with the same contact angle.

Chapter 4. Bubble Physics Measurements

In order to understand the bubble behaviors in the real boiling environments, a pool boiling experiment is performed. Time-lapse images for bubble evolution are captured by a high-speed camera. Bubble departure diameters, bubble periods, and wall heat fluxes from experimental and numerical results are compared and discussed in this chapter.

4.1 Description for the Experiment Setup

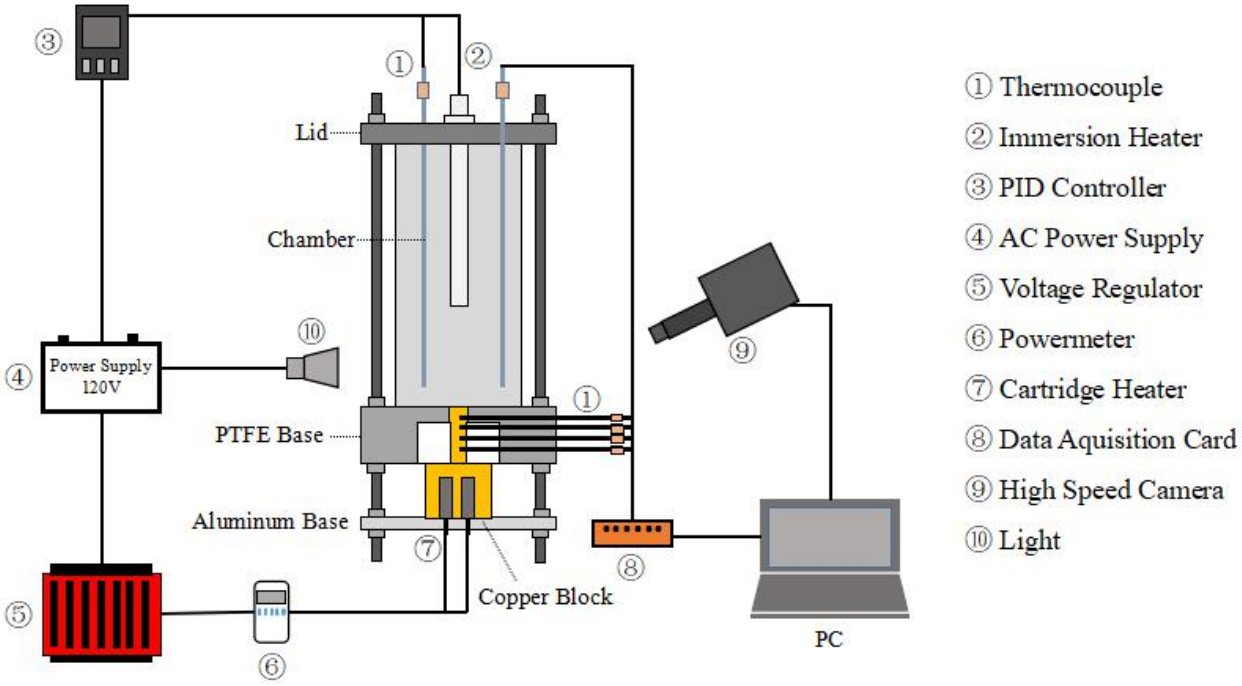

Figure 4-1. Schematic view of pool boiling experiment setup.
Photos for bubble behaviors are taken from the high-speed camera.

To further understand the bubble behavior under pool boiling conditions, we prepare a pool boiling experiment setup, which is shown in figure 4-1. Deionized water with 15min degassing process is boiled in a 100mm×100mm×200mm transparent polycarbonate chamber. The boiling chamber is supported by a PTFE base whose melting point is 280°C. Heat is generated from four 200W cartridge heaters and conducted upward into a 10mm ×10mm square copper heating surface. An aluminum base with 12.5mm thickness is installed underneath the copper block in order to hold the whole boiling system. Four

thermocouples are inserted to obtain the copper temperature as well as calculate the heat flux. Positions for the four thermocouples are shown in figure 4-2, where T_1, T_2, T_3, and T_4 represent the temperature values from thermocouple number 1, 2, 3, and 4, respectively. d_2, d_3, and d_4 refer to the distance between two sequential thermocouples whereas d_1 is the length from the top surface of the copper block to the center point of the first thermocouple. Boiling heat flux is calculated by the following equation:

$$q'' = k_{Cu}\left[\frac{(T_4 - T_3)/d_4 + (T_3 - T_2)/d_3 + (T_2 - T_1)/d_2}{3}\right] \tag{25}$$

where k_{Cu} represents the thermal conductivity of copper, which is 400W/m·K. The sample, or heating surface, is attached to the copper block by solder paste (Delta, 618D) with a melting point 220°C. The temperature at the sample surface T_s is calculated based on:

$$T_s = T_{Cu} - q''\left(\frac{d_s}{K_s} + R''_{ITR}\right) \tag{26}$$

where d_s and K_s represents the thickness and thermal conductivity of the sample, respectively, and R''_{ITR} is the thermal resistance of the solder paste layer, whose value is 5×10^{-6}m^{2}K/W. The temperature at the copper block top surface T_{Cu} is defined based on the Fourier's Law:

$$T_{Cu} = T_1 - \left(\frac{T_4 - T_1}{d_2 + d_3 + d_4}\right)d_1 \tag{27}$$

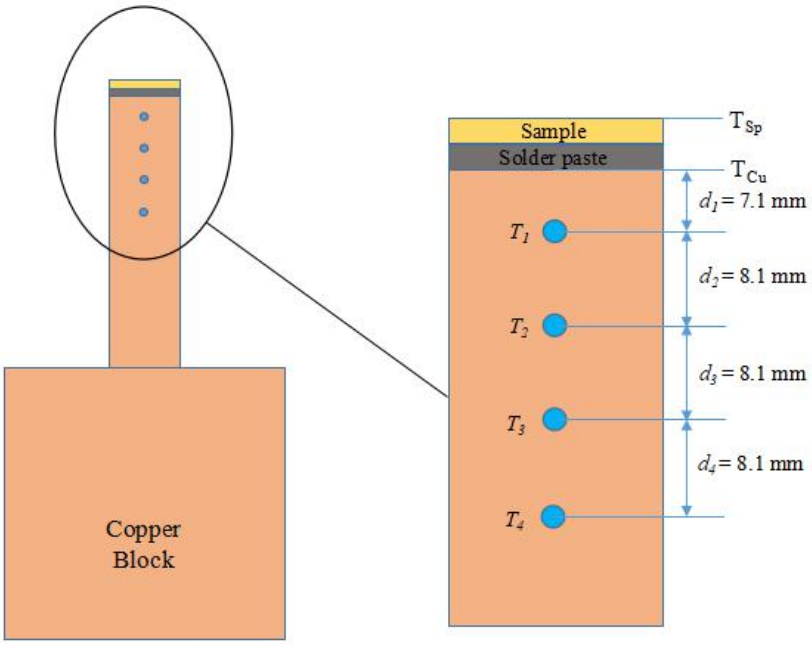

Figure 4-2. Copper block and the locations for thermocouples. Heat fluxes are calculated based on the temperature profile and locations.

In the measurement, the sample (heating surface) is selected to be bare brass with a contact angle of 96°. The thickness of this sample is 0.5mm. During the experiment, water saturation conditions are maintained by an immersion heater ②. The heat fluxes are controlled by a thermocouple ① coupled with the PID controller. Bubble behavior is captured and recorded by a high-speed camera (Photron: Fastcam Mini AX) with the frame rate of 2000 fps (frame per second).

4.2 Experiment Results and Discussion

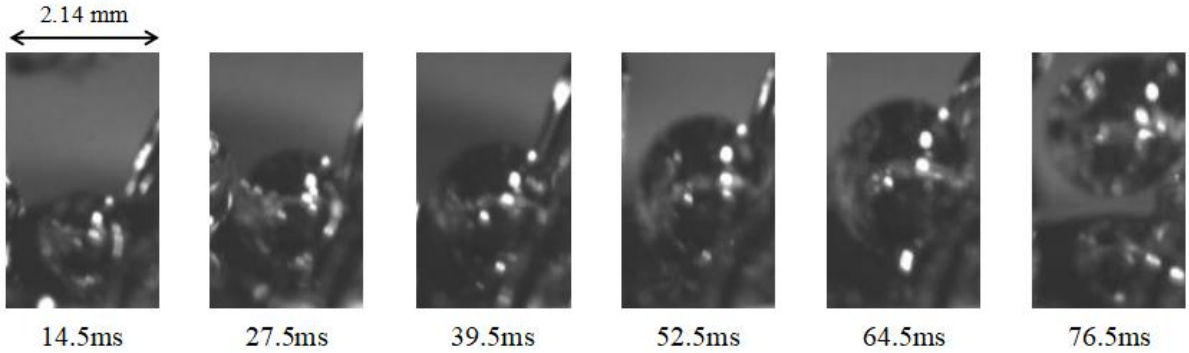

Figure 4-3. Time-lapse images showing bubble growth and departure. (wall heat flux: 94,488W/m^2; wall superheat: 12.6℃). Same bubble behaviors with a smaller bubble departure diameter and bubble period compared to CFD results.

Time-lapse images of bubble behaviors captured by a high-speed camera are shown in figure 4-3, where the corresponding wall heat flux and wall superheat are 94,488W/m^2 and 12.6°C, respectively. The sequence of photos is consistent with computed bubble behaviors under pool boiling conditions (figure 3-3 (a)-(e)). A detailed comparison between experimental results and numerical data is presented in table 4-1, where the experimental data shows that the bubble departs at a diameter around 2mm, which is smaller than the numerical results as well as Fritz's prediction.

In the pool boiling experiment, while the wall superheat reaches 10°C, several nucleation cavities are active at the same time. Bubbles grow from these active nucleation sites greatly accelerate the local flow field. Therefore, the wall heat flux in the experiment is much higher than the CFD results. The large wall heat flux also accelerates the bubble growth and departure processes, which leads to smaller bubble departure diameters, as well as shorter bubble periods.

Table 4-1. Comparison between numerical results and experimental data.

Form	Contact Angle (degree)	Departure Diameter (mm)	Bubble Period (ms)	Wall Heat Flux (W/m^2)
Numerical Results	90	6.09	132.77	30,631
Numerical Results	99	6.60	121.91	31,313
Experiment Data	96	2.10	76.25	94,488

Chapter 5. Summary and Conclusions

Numerical methods have been employed to model the bubble behaviors on both flat and pillar heating surfaces. The impacts of contact angle and different geometries on bubble dynamics such as bubble departure diameters, bubble periods, velocity fields, and wall heat fluxes have been investigated. Bubble evolution on pillar heating surface with a 90^o contact angle has also been numerically simulated in order to investigate the influence of surface structure to heat transfer performance. A pool boiling experiment has been performed to further study the bubble dynamic physics and verify the numerical results. The conclusions of this work are listed as follows:

A. On flat heating surfaces, bubble departure diameter increases linearly with contact angle in the range of 72^o-108^o, which is consistent with the Fritz model. Bubble departure diameters from this simulation have a larger value than the prediction of Fritz, which may due to the additional consideration about evaporation process at the contact line region. Disturbance triggered by flow field inside the contact line region increases surface heat flux as well as reduces the bubble period and the bubble departure diameter. Flow field around the contact line region is most stable while contact angle equals to 90^o, which may be a result of the maximum vertical surface tension component in this case.

B. On pillar surface, flow field around the pillar plays an important role to the bubble growing process. After bubble covers the pillar top surface, the near-pillar liquid flow constrains the bubble growth in the radial direction. In this case, the vapor bubble is forming into an oval-shape, which will in turn enhance the velocity field around the contact line region. Comparing to the bubble behaviors and heat transfer performance on the flat surface with the same contact angle, the enhanced flow field provides a larger wall heat flux, reduces the bubble departure diameter and the bubble period.

C. Under real pool boiling conditions, while the wall superheat is around 10^oC, several nucleation sites are active on a flat heating surface. Bubble nucleation, growth, and departure from these nucleation cavities effectively enhanced the local flow field, which

will in turn improve the wall heat flux. Bubble departure diameter, as well as its growth period, are reduced under higher wall heat fluxes due to the larger evaporation momentum force.

D. In order to further understand the impacts of surface characteristics on bubble behaviors as well as heat transfer performances, numerical investigations will be continued for the bubble behaviors on pillar surfaces with different contact angles. Boiling performances on flat and pillar heated surfaces will also be tested by using the pool boiling experiment setup. Numerical results accompanied by the experimental data will give a comprehensive understanding to explain the boiling performances with varying heated surface characteristics.

References

[1] V.K. Dhir, Boiling heat transfer, Annu. Rev. Fluid Mech., vol. 30, pp. 365-401, 1998.

[2] S. Nukiyama, The maximum and minimum values of the heat Q transmitted from metal to boiling water under atmospheric pressure, J. Jpn. Soc. Mech. Eng., vol. 37, pp. 367-374, 1934.

[3] Y.Y. Hsu, On the size range of active nucleation cavities on a heating surface, J. Heat Transfer, vol. 84, pp. 207–213, 1962.

[4] K. Mizukami, entrapment of vapor in reentrantcavities, Lett. Heat Mass Transfer, vol. 2, pp. 279–284, 1977.

[5] T.W. Forest, The stability of gaseous nuclei at liquid-solid interfaces, J. Appl. Phys., vol. 53, pp. 6191–6201, 1982.

[6] C.Y. Han, P. Griffith, The mechanism of heat transfer in nucleate pool boiling, Int. J. Heat Mass Transfer, vol. 8, pp. 887–914, 1965.

[7] B.B. Mikic, W.M. Rohsenhow, A new correlation of pool boiling data including the effect of heating surface characteristics, J. Heat Transfer, vol. 9, pp. 245–250,1969.

[8] N.R. Snyder, D.K. Edwards, Summary of conference on bubble dynamics and boiling heat transfer, Memo 20-137, Jet Propulsion Laboratory, pp. 14–15, 1956.

[9] M.G. Cooper, A.J.P. Lloyd, The microlayer in nucleate boiling, Int. J. Heat Mass Transfer, vol. 12, pp. 895–913, 1969.

[10] C.M. Voutsinos, R.L. Judd, Laser interferometric investigation of the microlayer evaporation phenomenon, J. Heat Transfer, vol. 97, pp. 88–92, 1975.

[11] L.D. Koffman, M.S. Plesset, Experimental observations of the microlayer in vapor bubble growth on a heated solid, Int. J. Heat Mass Transfer, vol. 5, pp. 625–632, 1983.

[12] B.M. Christopher, B.X. Wang, and X.F. Peng, Convection and evaporation of microlayer underneath bubbles under microgravity, Chin. J. Eng. Thermophys., vol. 19, pp. 193-197, 1998.

[13] G. Son, V.K. Dhir, Numerical simulation of nucleate boiling on a horizontal surface at high heat fluxes, Int. J. Heat Mass Transfer, vol. 51, pp. 2566-2582, 2008.

[14] W. Lee, G. Son, and J.J. Jeong, Numerical Analysis of Bubble Growth and Departure from a Microcavity, Numerical Heat Transfer: Part B, vol. 58, pp. 323-342, 2010.

[15] R.F. Gaenrtner, Photographic study of nucleate pool boiling on a horizontal surface, ASME J. Heat Transfer, vol. 87, pp. 17-29, 1965.

[16] P. Sadasivan, P.R. Chappidi, C. Unal, and R.A. Nelson, Possible mechanisms of macrolayer formation, Int. Comm. Heat Mass Transfer, vol. 19, pp. 801-815, 1992.
[17] A.K. Das, P.K. Das, and P. Saha, Heat transfer during pool boiling based on evaporation from micro and macrolayer, Int. J. Heat Mass Transfer, vol. 49, pp. 3487-3499, 2006.
[18] P. Stephan, J. Hammer, A new model for nucleate boiling heat transfer, Warme und Stoffubertragung, vol. 30, pp. 119-125, 1994.
[19] J. Kim, Review of nucleate pool boiling bubble heat transfer mechanisms, Int. J. Multiphase Flow, vol. 35, pp. 1067-1076, 2009.
[20] C.H. Wang, V.K. Dhir, Effect of surface wettability on active nucleation site density during pool boiling of water on a vertical surface, J. Heat Transfer, vol. 115, pp. 659-669, 1993.
[21] Y. Takata, S. Hidaka, J.M. Cao, T. Nakamura, H. Yamamoto, M. Masuda, and T. Ito, Effect of surface wettability on boiling and evaporation, Energy, vol. 30, pp. 209-220, 2005.
[22] A. Jaikumar, S.G. Kandlikar, Pool boiling inversion through bubble induced macroconvection, Appl. Phys. Lett., vol. 110, p. 094107, 2017.
[23] S.G. Kandlikar, Enhanced macroconvection mechanism with separate liquid - vapor pathways to improve pool boiling performance, J. Heat Transfer, vol. 139, p. 051501, 2017.
[24] C. Fang, M. David, A. Rogacs, and K. Goodson, Volume of fluid simulation of boiling two-phase flow in a vapor-venting microchannel, Frontiers in Heat and Mass Transfer, vol. 1, p. 013002, 2010.
[25] J.E. Kennedy, G.M. Roach, M.F. Dowling, S.I. Abdel-Khalik, S.M. Ghjaasiaan, and S.M. Jeter, The onset of flow instability in uniformly heated horizontal microchannels, J. Heat Transfer, vol. 122, pp. 118-125, 2000.
[26] L. Zhang, E.N. Wang, K. Goodson, and T. Kenney, Phase change phenomena in silicon microchannels, Int. J. Heat Mass Transfer, vol. 48, pp. 1572-1582, 2005.
[27] S. Garimella, An experimentally validated model for two-phase pressure drop in the intermittent flow regime for circular microchannels, J. Fluids Eng., vol. 124, pp. 205-214, 2002.
[28] P. Zhou, K. Goodson, and J. Santiago, U.S. Patent 6, 994, 151 B2, 2006.
[29] M.P. David, T. Khurana, C. Hidrovo, B.L. Pruitt, and K. Goodson, Vapor-venting, microchannel heat exchanger for electronics cooling, Proceedings of IMECE, Seattle, WA, 2007.

[30] S. Inada, Y. Miyasaka, R. Izumi, and Y. Owase, A study on boiling curves in subcooled pool boiling (1st Report, An effect of liquid subcooling on local heat transfer), Transaction of JSME, vol. 47, pp. 852–861, 1981.
[31] S. Inada, Y. Miyasaka, S. Sakumoto, et al., An effect of liquid subcooling on local heat transfer, Transaction of JSME, vol. 47, pp. 2021–2029, 1981.
[32] K. Suzuki, T. Kokubu, M. Nakano, H. Kawamura, I. Ueno, H. Shida, and O. Ogawa, Enhancement of heat transfer in subcooled flow boiling with microbubble emission, Exp. Thermal and Fluid Science, vol. 29, pp. 827-832, 2005.
[33] K. Suzuki, F. Inagaki, and C. Hong, Subcooled boiling in the ultrasonic field-on the cause of microbubble emission boiling, Heat Transfer Eng., vol. 32, pp. 673-682, 2002.
[34] K. Suzuki, K. Torikai, H. Satoh, J. Ishimaru, and Y. Tanaka, Boiling heat transfer in a horizontal rectangular channel: Observation of MEB and MEB generation, Heat Transfer-Asian Research, vol. 30, pp. 426-438, 2001.
[35] S. Kumagai, R. Kubo, and T. Kawasaki, Micro-bubble emission boiling from horizontal and vertical surfaces to subcooled parallel flow water, Heat Transfer-Asian Research, vol. 32, pp. 130-140, 2003.
[36] J. Tang, G. Zhu, and L. Sun, Microbubble emission boiling in subcooled pool boiling and the role of Maragoni convection in its form, Exp. Thermal Fluid Sci., vol. 50, pp. 97-106, 2013.
[37] C. Kunkelmann, P. Stephan, Numerical simulation of the transient heat transfer during nucleate boiling of refrigerant HFE-7100, Int, J. Refrigeration, vol. 33, pp. 1221-1228, 2010.
[38] A. Mukherjee, S.G. Kandlikar, Numerical simulation of growth of a vapor bubble during flow boiling of water in a microchannel, Microfluid Nanofluid, vol. 1, pp. 137-145, 2005.
[39] A. Mukherjee, S.G. Kandlikar, Numerical study of single bubbles with dynamic contact angle during nucleate pool boiling, Int. J. Heat Mass Transfer, vol. 50, pp. 127-138, 2007.
[40] Z. Chen, Y. Utaka, On heat transfer and evaporation characteristics in the growth process of a bubble with microlayer structure during nucleate boiling, Int. J. Heat Mass Transfer, vol. 81, pp. 750-759, 2015.
[41] J. Murallidharan, G. Giustini, Y. Sato, B. Niceno, V. Badalassi, and S.P. Walker, Computational fluid dynamics simulation of single bubble growth under high - pressure pool boiling conditions, Nuclear Eng. Technol., vol. 48, pp. 859-869, 2016.

[42] C.R. Kharangate, I. Mudawar, Review of computational studies on boiling and condensation, Int. J. Heat Mass Transfer, vol. 108, pp. 1164-1196, 2017.
[43] F. Gibou, L. Chen, D. Nguyen, and S. Banerjee, A level set based sharp interface method for the multiphase incompressible Navier-Stokes equations with phase change, J. Comput. Phys., vol. 222, pp. 536–555, 2007.
[44] R.W. Schrage, A Theoretical Study of Interphase Mass Transfer, Columbia University Press, New York, 1953.
[45] W.H. Lee, A pressure iteration scheme for two-phase flow modeling, in: T.N. Veziroglu (Ed.), Multiphase Transport Fundamentals, Reactor Safety, Applications, vol. 1, Hemisphere Publishing, Washington, DC, 1980.
[46] C.W. Hirt, B.D. Nichols, Volume of fluid (VOF) method for the dynamics of free boundaries, J. Comput. Phys., vol. 39, pp. 201-225, 1981.
[47] H.L. Wu, X.F. Peng, P. Ye, and Y. Eric Gong, Simulation of refrigerant flow boiling in serpentine tubes, Int. J. Heat Mass Transfer, vol. 50, pp. 1186–1195, 2007.
[48] S.C.K. De Schepper, G.J. Heynderichx, and G.B. Marin, Modeling the evaporation of a hydrocarbon feedstock in the convection section of a steam cracker, Comput. Chem. Eng., vol. 33, pp. 122–132, 2009.
[49] Z. Yang, X.F. Peng, and P. Ye, Numerical and experimental investigation of two phase flow during boiling in a coiled tube, Int. J. Heat Mass Transfer, vol. 51, pp. 1003–1016, 2008.
[50] H. Lee, D.D. Agonafer, Y. Won, F. Houshmand, C. Gorle, M. Asheghi, and K. Goodson, Thermal modeling of extreme heat flux microchannel coolers for GaN-on-SiC semiconductor devices, Journal of Electronic Packaging, vol. 138, p. 010907, 2016.
[51] H. Lee, C.R. Kharangate, N. Mascarenhas, I. Park, and I. Mudawar, Experimental and computational investigation of vertical downflow condensation, Int. J. Heat Mass Transfer, vol. 85, pp. 865-879, 2015.
[52] J.U. Brackbill, D.B. Kothe, and C. Zemach, A continuum method for modeling surface tension, J. Comput. Phys., vol. 100, pp. 335-354, 1992.
[53] N.B. Vargaftik, B.N. Volkov, and L.D. Voljak, International tables of the surface tension of water, J. Phys. Chem. Ref. Data, vol. 12, pp. 817-820, 1983.
[54] S. Patankar, Numerical Heat Transfer and Fluid Flow, Hemisphere, New York, 1980.

[55] S.C. Cho, Y. Wang, K.S. Chen, Droplet dynamics in a polymer electrolyte fuel cell gas flow channel: Forces, deformation, and detachment. I: Theoretical and numerical analyses, J. Power Sources, vol. 206, pp. 119-128, 2012.

[56] S.C. Cho, Y. Wang, K.S. Chen, Droplet dynamics in a polymer electrolyte fuel cell gas flow channel: Forces, deformation, and detachment. I: Comparisons of analytical solution with numerical and experimental results, J. Power Sources, vol. 210, pp. 191-197, 2012.

[57] S. Gong, P. Cheng, Lattice Boltzmann simulations for surface wettability effects in saturated pool boiling heat transfer, Int. J. Heat Mass Transfer, vol. 85, pp. 635-646, 2015.

[58] R.L. Mohanty, M.K. Das, A critical review on bubble dynamics diameters influencing boiling heat transfer, vol. 78, pp. 466-494, 2017.

[59] W. Fritz, Maximum volume of vapor bubbles, Physikalische Zeitschrift, vol. 36, pp. 379–384, 1935.

[60] J. Liu, G. Wang, L. Zhang, Y. Shi, H. Zhang, and S.C.Yao, Numerical simulation of single bubble boiling behavior, Propulsion and Power Research, vol. 6, pp. 117-125, 2017.

[61] M. Matkovic, B. Koncar, Bubble departure diameter prediction uncertainty, Science and Technology of Nuclear Installation, vol. 2012, p. 863190.

[62] A. Mukherjee, S.G. Kandlikar, Numerical study of single bubbles with dynamic contact angle during nucleate pool boiling, Int. J. Heat Mass Transfer, vol. 50, 127-138, 2007.

Appendix - User-Defined Functions

```
#include "udf.h"

/************************ PRE - PROCESSING ************************/
/* FOR PHASE CHANGE MODEL */
#include "mem.h"
#include "sg_mphase.h"
#define T_SAT 373.15
#define LAT_HT 2257600
#define coeff 1000.0

/* FOR PRESSURE PROFILE */
#define ZMAX  0.022
#define PGAUGE  0
#define RHOWT  960
#define g  9.81
/******************************************************************/

/********* PART ONE - MASS SOURCE TERM FOR LIQUID PHASE ********/
DEFINE_SOURCE(liq_src, cell, pri_th, dS, eqn)
{
 Thread *mix_th, *sec_th;
 real m_dot_l;
 mix_th = THREAD_SUPER_THREAD(pri_th);
 sec_th = THREAD_SUB_THREAD(mix_th, 1);

 if(C_VOF(cell, pri_th)<0.99 && C_VOF(cell, pri_th)>0.01)
 {
   if(C_T(cell, mix_th)>=T_SAT)
   {
     m_dot_l = -coeff*C_VOF(cell, pri_th)*C_R(cell, pri_th)*
```

```
            fabs(C_T(cell, pri_th) - T_SAT)/T_SAT;
      dS[eqn] = -coeff*C_R(cell, pri_th)*
      fabs(C_T(cell, pri_th) - T_SAT)/T_SAT;
     }
   else
    {
      m_dot_l = coeff*C_VOF(cell, sec_th)*C_R(cell, sec_th)*
            fabs(T_SAT-C_T(cell,mix_th))/T_SAT;
      dS[eqn] = 0.;
     }
  }
   else
 {
  m_dot_l=0;
  dS[eqn] = 0;
 }
 return m_dot_l;
}

/******** PART TWO - MASS SOURCE TERM FOR VAPOR PHASE ********/
DEFINE_SOURCE(vap_src, cell, sec_th, dS, eqn)
{
 Thread * mix_th, *pri_th;
 real m_dot_v;
 mix_th = THREAD_SUPER_THREAD(sec_th);
 pri_th = THREAD_SUB_THREAD(mix_th, 0);
 if(C_VOF(cell, pri_th)<0.99 && C_VOF(cell, pri_th)>0.01)
 {
    if(C_T(cell, mix_th)>=T_SAT)
  {
      m_dot_v = coeff*C_VOF(cell, pri_th)*C_R(cell, pri_th)*
```

```
            fabs(C_T(cell, mix_th) - T_SAT)/T_SAT;
      dS[eqn] = 0.;
    }
     else
    {
      m_dot_v = -coeff*C_VOF(cell, sec_th)*C_R(cell, sec_th)*
            fabs(T_SAT-C_T(cell,mix_th))/T_SAT;
      dS[eqn] = -coeff*C_R(cell, sec_th)*
        fabs(C_T(cell, sec_th) - T_SAT)/T_SAT;
    }
  }
  else
  {
   m_dot_v=0;
   dS[eqn] = 0;
  }
  return m_dot_v;
}
/****** PART THREE - ENERGY SOURCE TERM FOR BOTH PHASES ******/
DEFINE_SOURCE(enrg_src, cell, mix_th, dS, eqn)
{
  Thread *pri_th, *sec_th;
  real   m_dot;
  pri_th=THREAD_SUB_THREAD(mix_th, 0);
  sec_th=THREAD_SUB_THREAD(mix_th, 1);
  if(C_VOF(cell, pri_th)<0.99 && C_VOF(cell, pri_th)>0.01)
  {
     if(C_T(cell, mix_th)>=T_SAT)
    {
      m_dot = -coeff*C_VOF(cell, pri_th)*C_R(cell, pri_th)*
            fabs(C_T(cell, pri_th) - T_SAT)/T_SAT;
```

```
      dS[eqn] =  -coeff*C_VOF(cell, pri_th)*C_R(cell, pri_th)/T_SAT;
    }
  else
    {
     m_dot = coeff*C_VOF(cell, sec_th)*C_R(cell, sec_th)*
             fabs(T_SAT-C_T(cell,mix_th))/T_SAT;
     dS[eqn] = -coeff*C_VOF(cell, sec_th)*C_R(cell, sec_th)/T_SAT;}
    }
  else
 {
  m_dot=0.0;
  dS[eqn] = 0;
  }
   return LAT_HT*m_dot;
 }
/************ PART FOUR - PRESSURE PROFILE DEFINATION ***********/
DEFINE_PROFILE(pressure_prof,t,i)   /* Here t need to be determined */
{
   real x[ND_ND];
   real y;
   face_t f;
   begin_f_loop(f,t)
   {
     F_CENTROID(x,f,t);
     y = x[0];
     F_PROFILE(f,t,i) = PGAUGE + RHOWT*g*(ZMAX-y);
   }
   end_f_loop(f,t)
}
/*********************************************************************/
```